Understanding and Controlling Conjugated Polymer Conformation and Photophysics: From Single Molecules to Aggregates

Youngah (Karen) Kwon

Submitted in partial fulfillment of the
requirements for the degree of
Doctor of Philosophy
of the Graduate School of Arts and Sciences

COLUMBIA UNIVERSITY

2020

Abstract

Understanding and Controlling Conjugated Polymer Conformation and Photophysics: From Single Molecules to Aggregates

Youngah (Karen) Kwon

Conjugated polymers have been extensively studied over the past decades for their potential use in modern optoelectronic devices such as organic solar cells and light-emitting diodes. However, due to their multichromophoric nature, the relationship between conformation and photophysical properties of conjugated polymers is still largely obscure, especially on the molecular and mesoscopic length scales, where deeper understanding is needed to improve device efficiency. In this dissertation, using poly[2-methoxy-5-(2-ethylhexyloxy)-1,4-phenylenevinylene] (MEH-PPV) and wide-field single-molecule fluorescence microscopy, we investigate the relationship between conformation and photophysics both on the single-molecule and aggregate levels, towards developing control over these properties. In Chapter 2, we explore how complex photophysical behaviors of conjugated polymer single molecules can complicate the interpretation of experimental results of a commonly used technique, fluorescence polarization modulation depth (M) measurements, which indirectly reports on molecular conformation. Through fluorescence imaging and simulations, we show that the sublinear relationship between excitation intensity and conjugated polymer photoluminescence decreases measured M values, especially in molecules with highly ordered conformations. These findings show that analysis of M measurements should be done with caution. In Chapter 3, first we examine the effect of solvent vapor annealing on MEH-PPV single-molecule conformation. We show that molecular conformation initially set by the dissolving solvent is preserved after solvent vapor annealing, even though molecular mobility is

observed during the process. Then, solvent vapor annealing is applied to high-concentration MEH-PPV samples to produce aggregates consisting of a few to hundreds of single molecules. We show that single-molecule conformation acts as a template for the aggregates. In addition, although the aggregates prepared in this work are largely isotropic, photoluminescence spectra indicate that exciton diffusion in these aggregates is enhanced over short length scales. In general, this work suggests techniques and approaches to enhance understanding of various photophysical phenomena in conjugated polymers and other multichromophoric systems over an array of length scales.

Table of Contents

List of Figures

Acknowledgments

First and foremost, my sincerest thanks goes to my advisor, Prof. Laura Kaufman, for her guidance and support over the years. Without her patience and generosity, I wouldn't be where I am at today. I am always in awe of her vast knowledge on a wealth of topics (I've been under her wing for the past five years, and yet, I still can't quite figure out how she can switch from discussing conjugated polymers to breast cancer cells in seconds.) She encouraged me to be an independent thinker and a researcher, to which I am forever grateful. My gratitude also goes to Prof. Wei Min for serving on my committee throughout the years. In addition, I thank Prof. Milan Delor, Prof. Latha Venkataraman, and Prof. Sanat Kumar for serving on my dissertation defense committee during this critical period of my graduate studies.

I'd also like to thank former and current Kaufman group members for being good companions throughout my journey towards Ph.D. Having started the program in the same year, Dr. Alyssa Manz and I have spent many hours talking about everything from research to dating, and I couldn't have asked for a better friend to spend the past five years with. Dr. Dat Tien Hoang has been a supportive figure, not only to my research but also to life in general, and I'm grateful for our continuing friendship. My gratitude also goes to Prof. Keewook Paeng for being a source for infinite amount of knowledge. I'm also thankful for Prof. Heungman Park, whose passion toward science has been a great motivator. I especially thank him for teaching me Python from the very basics. I thank Prof. Khanh-Hoa Tran-Ba for his positive outlook on life. Thank you, also, to Dr. Hyung Jun Park for being an excellent discussion partner, and Nicole Mandel for being a great office mate. Han Yang has been a great addition to our lab, and I thank her for asking many poignant questions that challenge me. And last but not least, Prof. Jaesung Yang and I have spent

a lot of time together, both in the lab, working late nights, and outside of the lab, attending various sports games. I thank him for being not only a great mentor but also a great friend.

I have also met a lot of great people in the chemistry department, who I would like to thank. My gratitude goes to Dr. Jaeeun Yu for listening to me whine about everything graduate school. I'd also like to thank Dr. Leslie Hamachi for being a wonderful friend, helping me settle into Columbia when I first arrived. I'm also grateful for Patrick Saitta and Dr. Alex Radtke, whose friendships I value. In addition, though I won't name them individually, I'm especially thankful for everyone in my year, as they have been such good friends since the beginning. I enjoyed all our shenanigans throughout the past five years, and my graduate school experience wouldn't have been the same without them.

I also have been fortunate enough to have many great friends outside of Columbia Chemistry. Dr. Christine Kim and Juyoun Yoo have been my friends since middle school, and somehow we all ended up on the other side of the globe, pursuing Ph.D.'s in science; I'm thankful to have had them by my side in this journey. I'm also lucky to have a continuing friendship with Sun Dongbang, one of my closest friends from college, who started her own Ph.D. journey at a program that is only two-hour train ride away. I'd like to thank Chelsea Harris for being a great friend and a patient roommate. Navigating life in New York was much easier with her help. I also want to thank Prof. Miso Kim, Prof. Yunmi Choi, and Dr. Hyeri Lee for being great study buddies; my productivity has skyrocketed since working with them, and I'm forever thankful for their endless encouragements. My gratitude also goes to Hyo Jung Kim, whose friendship I deeply cherish.

Moving to a foreign country to attend graduate school wouldn't have happened without the support of people back at home. I want to thank my previous advisor Prof. Sungnam Park for

showing me what unwavering enthusiasm toward science looks like, which got me excited about research and eventually made me pursue a Ph.D. of my own. I'd also like to thank my parents for supporting all my endeavors. I want to thank my closest friends back home as well—Jisoo Han, Gowoon Kim, Ji-Yoon Lee, and Dr. Chiho Lee—for their unwavering love and support from afar.

Last but not least, I'd like to thank my husband, Carson Groenewold, for his unconditional love and support. I wouldn't have made it this far without you. You are the greatest life partner that anyone could ever ask for, and I am so lucky to have you in my life.

Dedication

To Carson,

for showing me the amount of love and support that I didn't think was possible.

Chapter 1. Introduction

1.1 Conjugated Polymers: Overview

1.1.1 Basics of Conjugated Polymers

Conjugated polymers have alternating single- and double-bonds that form a backbone along the molecule (Figure 1a). The carbon atoms in a conjugated polymer have hybridized sp^2 orbitals and p_z orbitals, and overlap of the p_z orbitals causes conjugated polymers to form an extended π-system along the backbone, where electrons are delocalized.[1,2] In the ground state, electrons occupy the orbitals of lowest energy. Figure 1b depicts the highest occupied molecular orbital (HOMO) and lowest unoccupied molecular orbital (LUMO). The energy gap between the HOMO and LUMO is what makes conjugated polymers attractive to researchers. Many conjugated polymers have a HOMO–LUMO energy gap in the range of 1.5–3.5 eV; therefore, they are able to absorb and emit light in the visible range of the spectrum.[1,3]

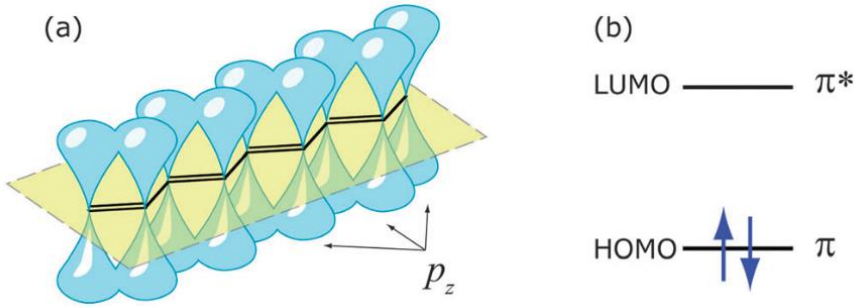

Figure 1. (a) Schematic depicting a conjugated molecular backbone. Overlapping p_z orbitals are shown in blue. (b) HOMO and LUMO showing two electrons in the HOMO with paired spins. (This figure is reproduced from reference 1 with permission from the publisher.)

Due to their unique capability for absorbing and emitting visible light, conjugated polymers have been molecules of interest for use in optoelectronic devices such as organic solar cells,[4–7] light-emitting diodes,[8–10] and field-effect transistors.[11,12] In organic solar cells, conjugated polymers are used in the active layer, typically in the form of bulk heterojunction, acting as

electron-donors and often mixed with fullerene derivatives, which act as electron-acceptors.[4,13,14] In contrast, in organic light-emitting diodes, conjugated polymers are used as the source of fluorescence in the form of an emitting layer.[8,10] The versatility of conjugated polymers partly originates from the side-chains attached to the backbone, as these can improve the solubility in organic solvent, as well as affect polymer packing and energy levels, resulting in different photophysical properties.[15–21] Moreover, the solution processibility of conjugated polymers translates to low production cost and physical flexibility, enabling efficient mass production and integration into devices.[3]

There are a number of conjugated polymers that have been studied extensively, with poly[2-methoxy-5-(2-ethylhexyloxy)-1,4-phenylenevinylene] (MEH-PPV) and poly(3-hexylthiophene) (P3HT) as two such examples (Figure 2). Both polymers emit fluorescence of yellowish red color, though the color varies depending on the molecular weight and the sample preparation conditions. Both MEH-PPV and P3HT are derivatives of the broader class of poly(*p*-phenylene vinylenes) (PPV) and polythiophenes with side-chains added to increase solubility without significantly altering other properties.

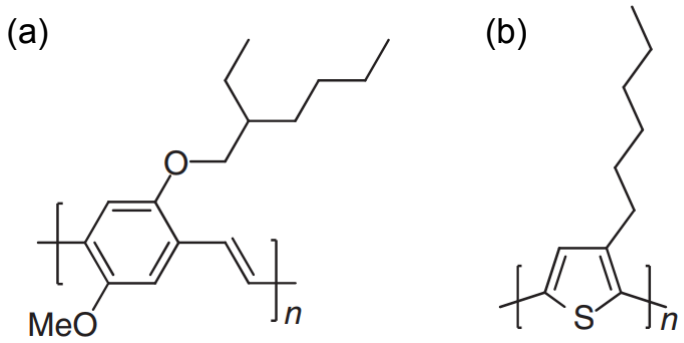

Figure 2. The chemical structures of (a) MEH-PPV and (b) P3HT.

When conjugated polymers absorb photons, instead of generating free charge carriers (i.e. electrons and holes), it generates excitons, which are (electronically neutral) Coulombically bound electron and hole pairs.[1,22–24] When created, the initial net spin of an exciton is zero, making it

singlet; but the excitation can undergo intersystem crossing, transforming to a triplet exciton.[1] For excitons to be useful in devices, both their lifetime and diffusivity are important. For solar cells, the exciton generated by the absorption of a photon must travel to the interface between the electron-donor and electron-acceptor layers so that the exciton can dissociate into charge carriers to generate electricity. As such, long-length scale diffusion without quenching is important for excitons in this scenario.[1] For light-emitting diodes, an electron and a hole must recombine to generate excitons in the emitting layer consisting of the conjugated polymer, with those excitons then radiatively decaying and emitting fluorescence.[25] Here, short-range migration of the exciton is preferred, so as to avoid potential non-radiative decay of excitons.[3]

Because conjugated polymer chains are relatively flexible and contain physical and potentially chemical defects, such as torsional, tetrahedral, or *cis* defects, conjugation does not extend across the entire chain and the "conjugation length" is significantly shorter than the chain length.[26–33] The individual regions over which delocalization occurs are considered "chromophores," as they act as the base units for absorption and emission. The length of a chromophore is considered to be 5–20 repeat units in MEH-PPV and 6–8 in P3HT, which have been determined by computational studies and spectral data comparison with oligomers.[17,34–38] As such, both MEH-PPV and P3HT — as well as other conjugated polymers — are multichromophoric. The presence of multiple chromophores on single chains complicates the photophysical properties of conjugated polymers; especially in a device context, where conjugated polymer chains exist in high concentration, detailed information on how chromophores interact with each other is obscured.

One of the factors determining the length of a chromophore is the quality of the solvent that the conjugated polymer is dissolved in, which determines the morphology of conjugated

polymer. The Flory–Huggins theory compares the interaction between the polymer and the solvent with those between the polymer and solvent molecules themselves.[39] The difference between the enthalpies is represented via the polymer–solvent interaction parameter χ. Solvents are referred as either good or poor (bad), indicating polymer-specific solubility depending on the value of χ; the smaller the χ, the better the solvent.[39] When a polymer is dissolved in a good solvent, since the polymer chain prefers to interact with the solvent rather than itself, the chain tends to have a more open conformation. On the other hand, when a polymer is dissolved in a poor solvent, the polymer prefers to interact with itself rather than with the solvent surrounding it, and the chain may collapse into a tightly coiled conformation. In dynamic light scattering measurements of MEH-PPV in solutions, the difference in polymer hydrodynamic radii can be seen as a function of solvent (Figure 3). Here, chlorobenzene (CB) is a good solvent and tetrahydrofuran (THF) is a poor solvent; the polymer's hydrodynamic radius is smaller when it is dissolved in a poor solvent. From here forward, this introduction will continue to draw examples from the literature on MEH-PPV, as that is the conjugated polymer under study in the later chapters of this dissertation.

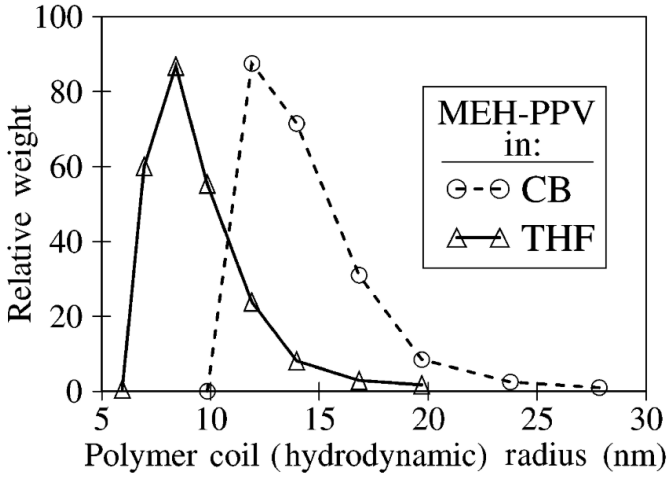

Figure 3. Hydrodynamic radii measured with dynamic light scattering for solutions of MEH-PPV (M_w = 535 kDa). (This figure is reproduced from reference 32 with permission from the publisher.)

The morphology as determined by sample preparation conditions, including the dissolving solvent, and the resulting distribution of chromophores, are reflected in the absorption and emission spectra (Figure 4). The absorption spectrum is broad and featureless, indicative of a broad spread of conjugation lengths present in the sample.[32,40] In contrast, finer features are observed in the emission spectrum, which is red-shifted compared to the absorption spectrum. Researchers have concluded that the vibronic features, as well as the Stokes shift, reflect energy transfer to low-energy sites present on the conjugated polymer chains where the conjugation length is relatively long, inferred from the "particle-in-a-box" model.[32,40,41]

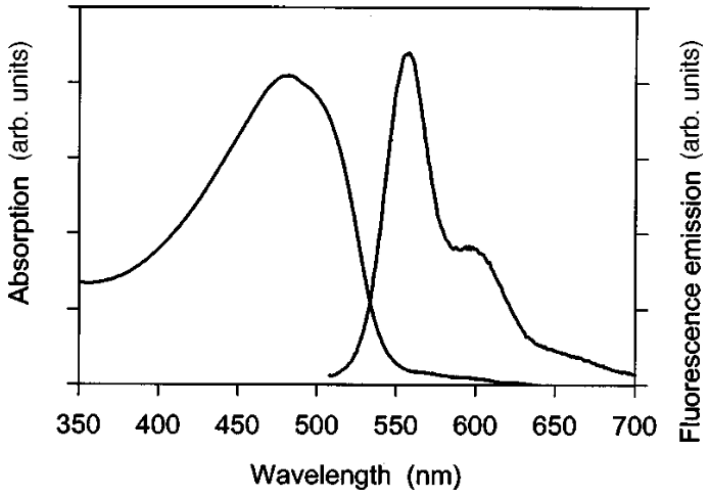

Figure 4. Absorption and photoluminescence (PL) spectra of MEH-PPV in toluene. (This figure is reproduced from reference 42 with permission from the publisher.)

1.1.2 Energy Transfer between Chromophores

Researchers have determined via a variety of approaches such as site-selective fluorescence spectroscopy that the multichromophoric nature of conjugated polymers leads to facile "downhill" energy transfer, such that the generated excitons migrate towards a small number of chromophores with longer conjugation length and lower energy.[43,44] The findings were later confirmed by single-molecule studies, which will be discussed later in the Introduction.

Two types of incoherent energy transfer were suggested for conjugated polymers: Förster and Dexter.[1,24,45,46] Förster energy transfer, which is often described as "through-space" energy transfer, is the dominant energy transfer type in interchain interactions (Figure 5a).[24] The factors influencing this type of energy transfer are overlap between donor emission and acceptor absorption spectra, donor–acceptor distance, and their mutual orientation.[47] The energy transfer rate is sensitive to the donor–acceptor distance (r), as it depends on $1/r^6$, and the transfer is typically observed over length scales of r ~ 1–5 nm for a single-step process.[1] Dexter energy transfer, in contract, is described as "through-bond" energy transfer, where an actual exchange of electrons take place (Figure 5b).[1] The energy transfer in this case can only occur at short distances (~ 1 nm), where there is a significant orbital overlap.[46] While both singlet and triplet excitons can be transferred via Dexter energy transfer, Förster energy transfer has higher efficiency in singlets.[1]

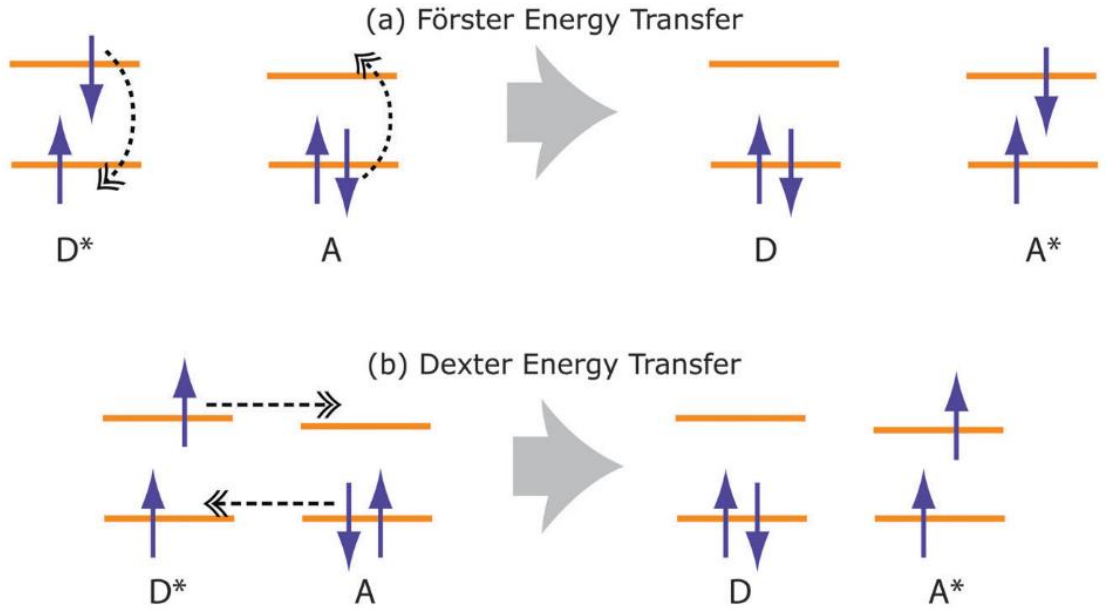

Figure 5. Schematics depicting (a) Förster energy transfer and (b) Dexter energy transfer. The horizontal lines represent HOMO and LUMO energy levels of donor (D) and acceptor (A) molecules; the asterisk denotes excited state. The dashed arrows represent simultaneous rearrangement of the electronic configuration. (This figure is reproduced from reference 1 with permission from the publisher.)

In addition to the types of incoherent energy transfer described above, coherent energy transfer was recently observed in a conjugated polymer using an ultrafast experimental technique.

When electronic and vibrational couplings are comparable, as may be the case in conjugated polymer systems, the system is in the intermediate coupling regime: in this regime, fast intrachain energy transfer via coherent processes can occur, providing a supplementary pathway for energy transfer in addition to the incoherent hopping transfer between chain segments.

1.1.3 Quenching Processes in Conjugated Polymers

Exciton quenching processes and relaxation mechanisms in MEH-PPV have not been fully elucidated. However, this is an active area of study given that such processes greatly influence device function. One of the major sources of quenching is photooxidation by molecular oxygen.[48–52] When a vinyl group is present in a conjugated polymer such as PPV and its derivatives, molecular oxygen can break the vinyl bond, creating keto-defects.[24,49] In addition, molecular oxygen – whose electronic ground state is a T_0 state – can react with triplet exciton to create singlet oxygen, which can then attack the π-bond in the conjugated polymer as it is chemically very reactive. In addition to molecular oxygen, radical cations and anions have been suggested as efficient quenchers of the fluorescence.[53]

Other processes that permanently quench fluorescence emerge from excitons interacting with themselves or charge carriers, as excitons are mobile.[24] There are several varieties of these exciton annihilation processes depending on the type of excitons involved: singlet–singlet, singlet–triplet, and triplet–triplet.[24,47,54–56] Though the details of the processes are distinct, they are all undesirable, especially for organic light-emitting diodes as such annihilation processes lead to lesser degree of fluorescence emission than theoretically possible.

1.2 Single-Molecule Fluorescence Microscopy

1.2.1 Basics of Single-Molecule Fluorescence Microscopy

The need for single-molecule studies of conjugated polymers became clear as ensemble measurements proved difficult to interpret due to the multichromophoric nature of the molecules and various factors including chain-to-chain interactions, local aggregation, and morphological heterogeneity in the conjugated polymer layer.[57,58] By performing experiments on a single-molecule level, researchers were able to observe a distribution of molecules, not an ensemble average from condensed phase samples. It is worth noting, however, that interpretation of single-molecule experimental results are not always straightforward, as even in a single chain, multiple chromophores exist, often more than a hundred in number.

There are two popular methods for single-molecule fluorescence microscopy: confocal and wide-field.[57] In this dissertation, we focus on wide-field microscopy, as that is the chosen method of our lab. Detailed optical setups used in our work will be provided in each of the following chapters. Regardless of particular optical approach, for single-molecule studies, conjugated polymer chains of interest are typically isolated and immobilized. Many single-molecule measurements on conjugated polymers, including the ones described in this dissertation, achieve this by immobilizing the conjugated polymers of interest in an inert host polymer matrix that lacks fluorescence signal in the spectral region where the conjugated polymer would emit.[41,57,59] Some of the most commonly used host polymers in conjugated polymer single-molecule experiments are polystyrene (PS), poly(methyl methacrylate) (PMMA), polyvinyl alcohol (PVA), and Zeonex.[57,60] Typically, a dilute solution of the conjugated polymer is mixed with a host polymer solution, and the mixture is spin-coated onto a substrate of choice. Other methods such as drop-casting can be used, but spin-coating provides finer control over the film thickness than other approaches, making

this the preferred method. Finally, the prepared film sample containing well-separated conjugated polymers is observed using single-molecule fluorescence imaging and/or spectroscopy.

Optical imaging is generally subject to the diffraction limit: owing to the wave-like nature of light, emission from a point-source (in this case, a single chromophore) diffracts into a pattern known as a point spread function.[61] When the emitted light is collected by an objective lens and focused onto the imaging plane on a CCD camera (a detector for our purposes), the imaged feature shows concentric circles called Airy disks.[62] According to Abbe's law, diffraction limit is expressed as

$$d = \frac{\lambda}{2NA} \qquad \text{Eq 1}$$

Here, NA is the numerical aperture of the objective and λ is the wavelength of the light. This is also the smallest distance between two emitting sites for them to be distinguishable. This limits the microscope's resolution to about 250 nm, while the size of a conjugated polymer chain is much smaller.[63] Thus, multiple emitters on a conjugated polymer chain that is multichromophoric cannot be resolved even with single molecule approaches.

Despite these limitations, single-molecule fluorescence microscopy and spectroscopy have revealed information previously obscured by ensemble measurements. One important discovery was the connection between single-molecule conformation and photophysical properties. Even though general relationships between such polymers' morphology and photophysical properties had been studied previously, single molecule studies were able to tease out details of this relationship.

In the following sections, a number of single-molecule experimental techniques, their application on MEH-PPV, and results from such studies will be introduced. Aside from the first method, excitation polarization modulation measurement, which is an indirect way of measuring

single-molecule conformation, these techniques provide similar information. In particular, they show that "downhill" energy transfer occurs on a single-molecule level; in such a "funneling" process, the exciton migrates towards a few low energy sites that exist on a chain, regions where the conjugation length is longer or π-π stacking is present. Hence energy migration depends on chain conformation, which then dictates the photophysics we observe.

1.2.2 Fluorescence (Excitation) Polarization Modulation Depth Measurements

As described above, optical imaging of conjugated polymer chains, regardless of their molecular weight within a typical experimental range, will be constrained by the diffraction limit. As such, it will be impossible to trace out conjugated polymer conformation directly via optical imaging. As a result, researchers have developed indirect methods to detect single-molecule conjugated polymer conformation. One such method is fluorescence modulation depth (*M*) measurements, which are technically simple to perform and theoretically simple to interpret.[26] As such, this has been one of the most popular methods of assessing polymer chain conformation.[41]

This method uses the fact that difference in chain conformation leads to difference in absorption anisotropy. In a single chain, the sum of the transition dipole moments can be represented as an absorption ellipsoid, as shown in Figure 6a, with the assumption that the transition dipoles of a polymer chain are aligned with the polymer backbone. When linearly polarized excitation light is used, the fluorescence intensity of the single-molecule conjugated polymer then depends on the alignment between the projection of this ellipsoid on the *x*-*y* sample plane and the linear polarization of the excitation light. Therefore, by placing a motorized rotating linear polarizer in the excitation pathway, the fluorescence intensity from the conjugated polymer becomes a function of the polarization angle ϕ, as can be seen in Figure 6b. By fitting the intensity trajectory to $I(\phi) = I_0[1 + Mcos\{2(\phi - \phi_0)\}]$, the fluorescence modulation depth, *M*, can be

extracted for each molecule. Here, ϕ_0 is a reference polarization angle at the intensity maximum and I_0 is a reference fluorescence intensity at the intensity maximum. Theoretically, the M value varies from 0 to 1; if the transition dipoles are completely aligned, M will be 1, and if the transition dipoles are completely isotropic, M will be 0. While this technique is very useful, it must be noted that the projection of the sum of the transition dipole moments for each conjugated polymer chain, and thus the M value, is not unique for each conformation. Therefore, the distribution of M values in a sample as a histogram is often compared with results from Monte Carlo simulations of polymers approximated as bead-spring models.[26]

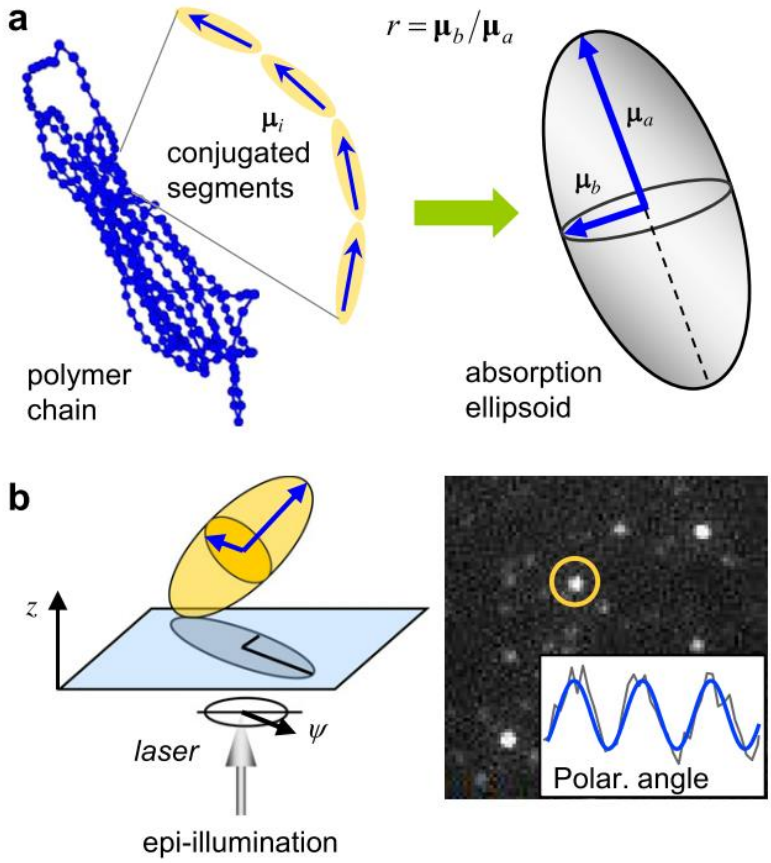

Figure 6. Principle of determining single conjugated polymer chain conformation by measuring absorption anisotropy. (a) Schematic relationship between chain conformation and absorption ellipsoid; (b) projection of the ellipsoid on the sample plane by epi-illumination (left) and a typical fluorescence image of single MEH-PPV chains (right). Inset: Excitation polarization angle modulated fluorescence intensity of the chain marked by circle in the image. (This figure is reproduced from reference 59 with permission from the publisher.)

Even though single-molecule measurements are not performed in the solution phase, nevertheless, the experimental results show that the effect of the solvent is carried over to the film, impacting chain conformation. When MEH-PPV single-molecule *M* measurements results are compared to the bead-on-a-chain Mote Carlo simulation results, depending on the solvent used in sample preparation, two categories of single-chain conformations emerge: ordered-collapsed and random coil. Figure 7 shows *M* measurement results from samples where MEH-PPV single-molecules embedded in PMMA host polymer matrix were prepared using two different solvents, toluene and chloroform, which are considered poor and good solvents for MEH-PPV, respectively. The sample spin-coated from a toluene solution shows an *M* distribution where the majority of values are close to 1, whereas the sample spin-coated from a chloroform solution shows a distribution shifted toward 0.

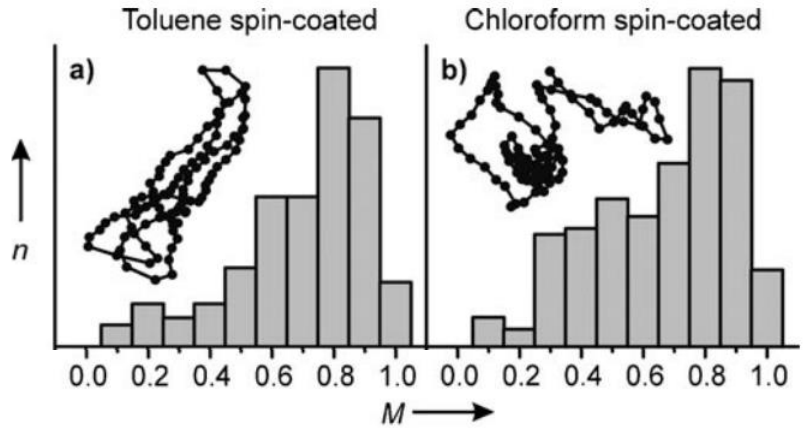

Figure 7. The modulation depth, *M*, histograms from single MEH-PPV molecules (M_n = 830 kDa) embedded in a PMMA host matrix, spin-coated from (a) toluene and (b) chloroform solution. The histograms consist of 152 and 230 MEH-PPV molecules for (a) and (b), respectively. The insets illustrate a conformation of the molecule consistent with the histograms. (This figure is reproduced from reference 64 with permission from the publisher.)

1.2.3 Fluorescence Intensity Transients

Additional information can be gained through monitoring fluorescence intensity of single conjugated polymer molecules over time. It is well accepted that excitons on conjugated polymers migrate to one or more chromophores with relatively low energy before emitting fluorescence.

With the development of optical techniques, exciton migration could be confirmed on a single-molecule level and (to a certain extent) visualized using optical methods. In particular, fluorescence intensity from single-chains as a function of time can be collected. If the system under observation is a single-chromophoric molecule that does not interact with another, the fluorescence intensity transient (or trajectory) would show only two levels: on and off. For conjugated polymers that are multichromophoric, however, the fluorescence intensity transients do not show simple two-level behavior. Rather, multiple levels of fluorescence intensity can be seen in these transients due to multiple emitters that are present on a single chain.

When MEH-PPV single-molecule samples were prepared in the two different solvents also depicted in the modulation depth experiments shown in Figure 7 and then spin-coated into the host polymer matrix to produce a film, MEH-PPV single-molecules showed distinct photobleaching patterns in their fluorescence intensity transients. In Figure 8, two representative fluorescence intensity transients are shown. When the sample is prepared in toluene, stepwise transients are typically found (Figure 8a), while when the sample is prepared in chloroform, exponential-like smooth decays are found (Figure 8b). These different patterns are indicative of two different exciton migration behaviors that are linked to two different single-chain conformations. In the ordered-collapsed conformation, which is more common among MEH-PPV single-molecules prepared in toluene, the interchain interactions are more frequent as a result of a higher number of chain-to-chain contacts. Therefore, the migration of photogenerated excitons to the low energy sites is well-facilitated and emission only occurs from the few chromophores with low energy. On the other hand, in a random coil conformation, which is more common in MEH-PPV single-molecules prepared in chloroform, intrachain exciton migration dominates as the number of chain-to-chain contacts is low compared to the ordered-collapsed conformation. Apparently, it is difficult

for excitons to migrate to low energy sites in this scenario and the emission occurs more randomly along the polymer chain from many different chromophores.

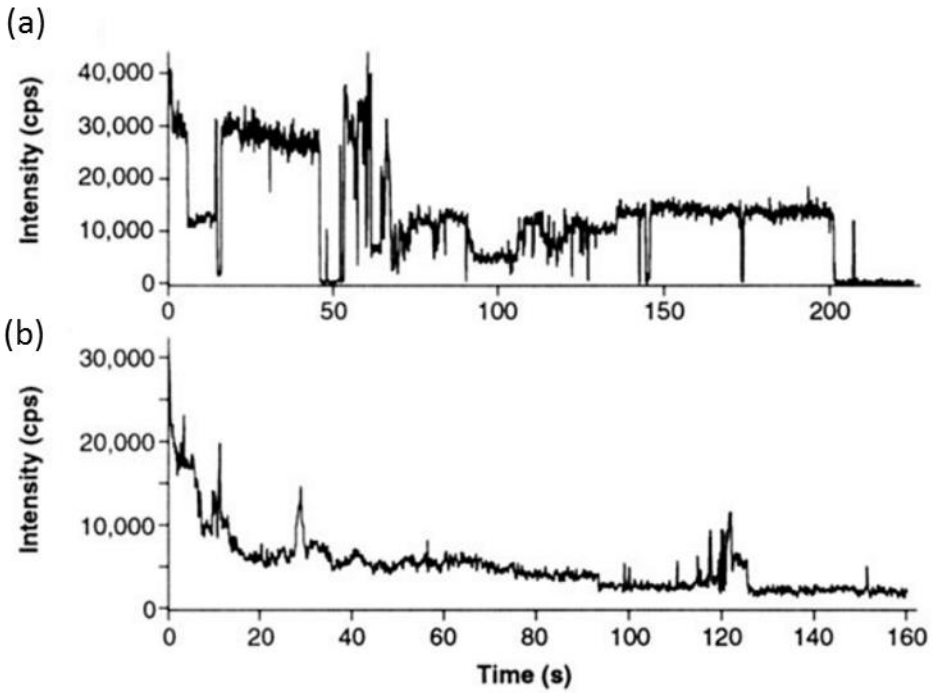

Figure 8. Representative fluorescence intensity transients for MEH-PPV (M_w = 1,000 kDa) single molecules embedded in polyvinyl butyral (PVB) host polymer matrix prepared in (a) toluene and (b) chloroform. (This figure is reproduced from reference 65.)

1.2.4 Single-Molecule Spectroscopy

In addition to single-molecule fluorescence microscopy, single-molecule spectroscopy has added information that could not be obtained from ensemble measurements. Spectra of single molecules showed the heterogeneous nature of polymer chains, even within the same sample. For conjugated polymer single-molecules, including MEH-PPV, especially in low-temperature spectral measurements, a bimodal distribution of the maximum fluorescence emission peaks is observed.[41,66,67] From this, spectra could be sorted into two categories, namely "red" and "blue." When the exciton migration to the single lowest energy site is well-facilitated, the emission of fluorescence occurs only from that single chromophore and a narrow, relatively red fluorescence spectrum is observed. On the other hand, if the emission is emerging from multiple chromophores

— meaning that the radiative decay is occurring not just from the lowest energy site but from other chromophores as well — the fluorescence spectrum may have relatively higher energy peaks.

1.2.5 Fluorescence (Emission) Polarization Modulation Depth Measurements

In addition to the polarization modulation depth measurements introduced above, simultaneous measurement of the excitation and emission polarization anisotropy can be performed to interrogate the energy transfer between chromophores by employing an additional linear polarizer before a detector.[21,68,69] When the polarization modulation depth of both excitation and emission were measured for MEH-PPV, increased *M* values for emission could be observed. The researchers concluded that this was due to energy transfer to the small number of regions of longer conjugation, which are the lower energy sites.[68,69] Barbara and co-workers were able to replicate these experimental results using simulations, confirming that including a small percentage of "red" sites, representing lower energy sites, in the simulation reproduced the bimodal nature of single-molecule MEH-PPV emission spectra measured experimentally.[68]

1.2.6 Photon Antibunching Measurement

Photon antibunching measurements are another type of single molecule approach that have been used to study conjugated polymers. Such measurements utilize the particle nature of light and the fact that a single emitter can only emit one photon at a time to determine whether an interrogated entity is a single emitter.[40] Light from the emitter passes through a beam splitter and temporal correlation between two detector signals is measured. If the coincidence rate is zero at zero delay, single photon emission is confirmed. Experiments on single molecules of MEH-PPV, initially dissolved in THF, revealed that highly folded MEH-PPV chains indeed fluoresce from a single emitting site, showing highly efficient interchain energy transfer.[70]

1.2.7 Super-Resolution Microscopy Techniques

While super-resolution techniques will not be discussed beyond this Introduction, it is worth mentioning recent technological developments in optical imaging that have enabled researchers to dissect conjugated polymer single-molecule photophysical behavior further. As discussed above, even though single-molecule techniques have provided us with tools to explore the heterogeneous nature of conjugated polymers, the presence of multiple chromophores on a single chain results in single molecule measurements that average over multiple emitting sites. With the development of super-resolution microscopy techniques, it became possible for researchers to look beyond the diffraction limit, and super-resolution techniques initially developed for biological systems were employed in conjugated polymer studies as well.[71]

One of the more commonly used super-resolution techniques in conjugated polymer studies involves combining localization microscopy with fluorescence intensity transients.[72] By photobleaching a single-molecule over time, emitters in a chain will be quenched one-by-one. Therefore, by localizing the emission with 2D Gaussian fitting to track the centroid position as emitters are being quenched, it becomes possible to map out the emitting sites in a single conjugated polymer chain, which were previously overlapping in a diffraction-limited spot.[59,72–74]

More recently, single-molecule high-resolution imaging with photobleaching (SHRImP) has been used on MEH-PPV by our group.[75] The localization method described above, though straightforward, has a limitation since the centroid position reports the average position of emitters. SHRImP employs image subtraction to localize each emitter. This work confirmed the inferred conformations of MEH-PPV molecules from earlier studies.

1.3 The Need to Go Beyond Single Molecules: Aggregates

While studying conjugated polymers on a single-molecule level revealed critical information on the relationship between polymer chain conformation and photophysical properties, single-molecule studies alone cannot provide a full picture of the photophysical behavior of these molecules, especially as they pertain to the device environment where intermolecular interactions are plentiful. To recapitulate aspects of the device environment while continuing to leverage advantages of single-molecule approaches that have been developed and fruitfully used to characterize conjugated polymers, researchers have performed experiments on aggregates consisting of a few to hundreds of conjugated polymer chains.[76,77,86,87,78–85]

Solvent vapor annealing (SVA) is a well-known technique for enhancing order in block copolymers and has recently been adapted for preparing conjugated polymer aggregates. In block copolymer studies, a film is typically exposed to solvent vapor, often in a crudely controlled manner. The solvent vapor enhances local mobility in the microphase-segregated film, which in turn enhances local segregation and order.[88–91] This method is now appreciated as a faster and less destructive alternative to thermal annealing, which entails applying heat to the film for a long periods of time and thus is accompanied by the possibility of unintentional sample degradation.[88,90]

To create conjugated polymer aggregates using SVA, first, a film consisting of conjugated polymers dispersed in an inert host polymer matrix is prepared. Then, the film sample is exposed to solvent vapor; often, a mixture of two solvent vapors, chosen depending on the conjugated polymer of interest and the host, is used to encourage the aggregation process.[76,83,85] For MEH-PPV in PMMA, a mixture of chloroform and acetone has been used. Chloroform, which is a good solvent for both components, swells the film and allows the MEH-PPV chains to become mobile. Acetone, on the other hand, is a good solvent for PMMA but a poor solvent for MEH-PPV,

encouraging MEH-PPV aggregation to limit contact with the acetone vapor. As in the case of block copolymers, the conjugated polymer chains gain mobility, which encourages the chains to self-assemble and aggregate via Ostwald ripening and coalescence.[80] Our lab has previously developed a home-built system for fine-control and monitoring of the SVA process using a quartz crystal microbalance and mass flow controllers. The details of the system can be found in Appendix A, as well as in reference 92.

The size and the conformation of the aggregates can be controlled in various ways; the first technique adapted was to control the ratio between chloroform and acetone in the vapor mixture. Other options were explored in subsequent years including altering the regioregularity or introducing defects or halogen atoms into the conjugated polymers during synthesis.[77,78,84] Our lab previously published that the initial concentration of the conjugated polymer in the host polymer matrix affects the size and the conformation of the resulting aggregates after the SVA process.[79] The same approaches used for single molecules described in the previous section have been used as single particle approaches to characterize aggregates. These studies have provided additional insight on the relationship between (intra and inter) chain order and photophysical properties, including those with more direct relevance to device properties.

1.4 Motivation and Dissertation Outline

Throughout the introduction, the importance of conjugated polymer conformation on its photophysical properties has been emphasized, and how that relationship can appear in experimental data was detailed. However, there are still obscurities in conjugated polymer conformation as reported through *M* measurements, which continue to be used due to their simplicity and convenience despite the development of super-resolution techniques. In addition,

the effects of the newly introduced use of solvent vapor annealing on conjugated polymers has not been fully explored. The rest of the dissertation will center around these issues.

In Chapter 2, we focus on *M* measurements, a commonly used technique to report on transition dipole alignment and thus molecular conformation of single conjugated polymers and aggregates, as discussed above. Extrapolation of conformation from these measurements, however, is complicated by the fact that photophysical processes (which themselves are coupled to conformation) may influence *M* values. In this chapter, we show that the presence of intensity-dependent partial photoluminescence quenching can suppress *M* values, with this suppression more prominent in molecules with highly aligned transition dipoles. We show that these effects are a direct consequence of properties of fluorescence intensity maxima and minima as a function of excitation polarization in MEH-PPV single molecules, as supported by a simulation that reproduces the experimental results. Our findings show that interpreting *M* values of molecules with complex photophysics should be done with caution.

In Chapter 3, first, we examine the possibility of MEH-PPV single-molecule conformation change by solvent vapor annealing. The single chains were prepared from two different solvents, toluene and chloroform, leading to different initial conformations, mainly ordered-collapsed and random coil. Then, solvent vapor swelling was performed using the same two solvents, resulting in four combinations. Even when the degree of swelling was large enough for single-chains to show mobility, we show that the initial conformation is maintained even after solvent vapor annealing, regardless of the type of solvent vapor used.

Then, to bridge the gap between single-molecule and bulk thin-film studies of organic semiconductors and understand the influence of molecular structure on photophysical properties across scales, we prepared and characterized aggregates containing a few to more than a thousand

single chains via well-controlled solvent vapor swelling of an inert polymeric matrix containing the conjugated polymer MEH-PPV. The single chains were initially immobilized in conformations with few interchain contacts, which can support exciton funneling on the single-molecule level. We show that aggregates prepared via solvent swelling and templated on such molecules result in largely isotropic aggregates. Analysis of aggregate polarization anisotropy, photoluminescence transient decay, and photoluminescence spectra as a function of aggregate size suggests that in these aggregates exciton diffusion is locally enhanced upon initial aggregation but does not reach extended length scales with further aggregation and annealing.

Chapter 2. Complex Photophysical Behaviors Affect Single Conjugated Molecule Optical Anisotropy Measurements

This chapter was reproduced in part from Kwon et al.[93]

2.1 Introduction

Optical anisotropy measurements have been widely used to characterize a variety of single molecules.[59,65,101,102,74,94–100] Among these techniques, fluorescence polarization modulation depth (*M*) measurements have been commonly applied to ascertain information on the conformation of single conjugated polymers and aggregates.[18,26,85,103–107,69,76–80,83,84] Although it is conceptually simple to understand why modulation depth measurements are closely connected to degree of alignment of transition dipoles and thus physical anisotropy of an interrogated molecule or aggregate, the interpretation of the value may be challenging, particularly in systems with complex photophysical behavior. Attempts to validate and strengthen information obtained from *M* measurements have come in the form of side-by-side experiment and modeling as well as experimental variations, in which both excitation and emission *M* values are measured.[26,68,69,108,109] Recently, we investigated how monitoring *M* values during photobleaching could reveal whether more compact or extended regions of the prototypical conjugated polymer poly[2-methoxy-5-(2-ethylhexyloxy)-1,4-phenylenevinylene] (MEH-PPV) were more photostable;[106] this work also clearly showed how partial photobleaching (and number of absorbing chromophores) itself affects measured *M* value for a molecule with static conformation. Here, we investigate a similar phenomenon, showing how *M* values may be suppressed in the presence of quenching processes, including those that have been suggested to be significant exciton quenching and de-excitation

mechanisms in MEH-PPV.[41,47,54,110–116] This phenomenon is analogous to one observed and described previously in bulk fluorescence anisotropy measurements on J-aggregates.[117,118]

Modulation depth can be measured by monitoring intensity of photoluminescence (PL) as a function of excitation and/or emission light polarization angle. In this study, excitation light polarization is modulated. M is typically defined as the normalized difference between the maximum and minimum intensities (I_{max} and I_{min}, respectively) of the PL curve as a function of light polarization.

$$M = \frac{I_{max} - I_{min}}{I_{max} + I_{min}} = \frac{A}{I_{ave}} \qquad \text{Eq 2}$$

where A is the amplitude of a sinusoidal modulation and I_{ave} is the mean intensity of the modulated signals (Figure 9a). Typically, modulation depth is obtained by fitting the PL curve as a function of polarization angle to

$$I_{PL} = C[1 + Mcos\{2(\varphi - \varphi_0)\}] \qquad \text{Eq 3}$$

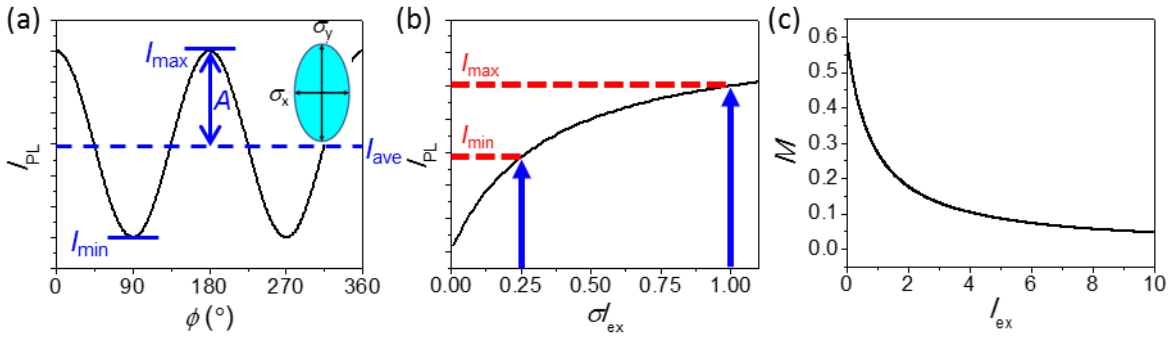

Figure 9. (a) Photoluminescence modulation curve used to calculate M for a simulated molecule with absorption cross-sections projected onto the sample plane of σ_x = 0.25 and σ_y = 1.0 (inset), with I_{min}, I_{max}, I_{ave}, and A as in Eq 2. (b) PL intensity as a function of excitation intensity (I_{ex}) for the example molecule described in (a) and with α = 10, β = 3 according to Eq 4. (c) Modulation depth (M) vs excitation intensity for the example molecule as defined by Eq 5.

with I_{PL} the intensity of photoluminescence, φ the polarization angle of the excitation light, φ_0 a reference polarization angle corresponding to the maximum intensity angle of the excitation polarization, and C a proportionality constant.

In conjugated polymers, absorption of photons is followed by creation of excitons, tightly bound electron–hole pairs. Even in single conjugated polymers, multiple excitons may be generated, and these may migrate to local minimum energy sites at which emission may occur. Such emission sites may become dark either permanently, after chromophores are affected by photobleaching, or temporarily, when an exciton occupies a long-lived state such as a triplet. Another mechanism by which temporary extinction of emission may occur is exciton–exciton annihilation. For multichromophoric conjugated polymers, exciton–exciton annihilation is expected to increase as a function of excitation intensity and polymer molecular weight.[55,109] Indeed, excitation intensity-dependent photoluminescence measurements showed that many conjugated polymer materials exhibit exciton–exciton annihilation and result in quenching at excitation power densities at and above ≈0.1 W/cm^2 at λ = 458 nm.[113] On the single-molecule level, this was shown for poly(3-hexylthiophene) (P3HT), where the PL increase deviates from a linear correlation with an excitation intensity ≈50 W/cm^2 at λ = 485 nm.[55]

Here, we consider how complex photophysical processes affect measured modulation depth using intensity-dependent exciton–exciton annihilation to illustrate the point. For both single and multichromophoric single polymers with exciton migration and intensity-dependent annihilation, PL intensity can be expressed by

$$I_{PL} = \frac{\alpha}{1 + \beta\sigma I_{ex}}\sigma I_{ex} \qquad \text{Eq 4}$$

where α is a proportionality factor related to internal quantum efficiency, σ is absorption cross-section, and β is a quenching factor.[55] In single P3HT molecules, it was shown that this form described observed PL intensity, consistent with singlet–triplet annihilation.[55] Although Eq 4 was used to describe molecular weight- and excitation intensity-dependent saturation in single P3HT molecules presumed to funnel all excitons to a single emitting site, this model can also serve as an effective expression for photoluminescence in molecules with multiple exciton domains such as MEH-PPV. In this case, in the absence of exciton domain coupling, quenching would occur in accordance with Eq 4 within each exciton domain, and the total photoluminescence intensity would be a sum of that from all domains, each described by Eq 4. This model would then be appropriate both for MEH-PPV molecules in ordered, collapsed conformations (with high M and few exciton domains) and those in more extended conformations (with low M and a greater number of exciton domains). More generally, we note that Eq 4 can describe quenching processes beyond singlet–triplet annihilation, and such quenching can emerge from a number of processes that involve exciton migration to long-lived quenching sites such as defects and charge traps.[47]

Within the model characterized by Eq 4, in the absence of quenching ($\beta = 0$), PL intensity is directly proportional to the absorption cross-section. For a molecule with $\sigma_x = 0.25$ and $\sigma_y = 1.0$, following from Eq 2 and Eq 4, $M = (\sigma_y - \sigma_x)/(\sigma_y + \sigma_x) = 0.6$, independent of excitation intensity. However, if β is nonzero and quenching occurs, M will be excitation intensity-dependent (except for molecules with $M = 0$ and 1) and assuming α and β are polarization independent, will vary as

$$M = \frac{\sigma_y - \sigma_x}{\sigma_x + \sigma_y + 2\beta\sigma_x\sigma_y I_{ex}} \qquad \text{Eq 5}$$

For M' measured at an excitation intensity cI_{ex}, with c greater than 1, $M' < M$ for the same molecule in the same conformation, and

$$M' = \frac{\sigma_x + \sigma_y + 2\beta\sigma_x\sigma_y I_{ex}}{\sigma_x + \sigma_y + 2c\beta\sigma_x\sigma_y I_{ex}} \times M \qquad \text{Eq 6}$$

The value of M' can also be expressed through a generalized form of Eq 2, via

$$M' = \frac{aI_{max} - bI_{min}}{aI_{max} + bI_{min}} \qquad \text{Eq 7}$$

If there is no excitation intensity-dependent quenching, co-efficients *a* and *b* will be identical and $M' = M$. However, if more quenching occurs at a higher excitation intensity, $a < b$ and $M' < M$. Assuming that α and β in Eq 4 are equal along the orthogonal *x* and *y* orientations of the molecule, $\alpha = 10$, and $\beta = 3$ in a molecule with $\sigma_x = 0.25$ and $\sigma_y = 1.0$, the *M* value will decrease from 0.54 to 0.27 for a relative excitation intensity increase of a factor of 10 ($I_{ex} = 0.1–1.0$) (Figure 9b,c). At low excitation intensity, PL intensity increases nearly linearly with excitation intensity, quenching is negligible, and the *M* value is close to 0.6. As excitation intensity reaches the regime in which quenching is evident, *M* falls rather rapidly to values typically associated with molecules lacking significant optical anisotropy. Such an excitation intensity-dependent *M* value change will be observed if emission intensity saturates with respect to increasing excitation intensity, regardless of particular source of quenching.

In this chapter, we confirm the effect of excitation intensity-dependent quenching on modulation depth measurements of single conjugated molecules with multiple exciton domains. The model system used is MEH-PPV single molecules dissolved in chloroform and confined in polystyrene since such molecules typically show broad *M* distributions,[106] which allows us to understand the effect as a function of initially measured modulation depth.

2.2 Experiment

2.2.1 Sample Preparation

MEH-PPV of M_n = 140 kDa and polydispersity index (PDI) = 1.8 was purchased from Polymer Source and was used without further purification. The MEH-PPV was diluted in ≈4 wt % polystyrene (M_W = 6.4 kDa, PDI = 1.05) with chloroform as the solvent. The solution was spin-cast onto native oxide-covered silicon wafers to prepare films of ≈200 nm thickness. The concentration of MEH-PPV in the solution was $\approx 10^{-11}$ M, and the average separation between molecules in the films was greater than 1 μm when imaged with wide-field microscopy.

2.2.2 Optical Setup

A home-built wide-field epifluorescence microscope system (Figure 10) was used to perform the experiments. Samples were placed in a vacuum cryostat held at ≈1 mTorr. A continuous wave laser at 532 nm (Spectra Physics; Millenia V, Nd:vanadate 532 nm diode laser) was the excitation source. Circularly polarized light was used for the excitation intensity-dependent PL measurement. Excitation intensity was increased from 20 W/cm^2 in increments of 20 W/cm^2 until excitation intensity reached 200 W/cm^2. Excitation intensity was then decreased in increments of 20 W/cm^2 until it reached the starting point of 20 W/cm^2. Ten frames were collected for each measurement at a frame rate of 5 Hz. The 10 frame average PL intensity was used for further data analysis. For *M* measurements, a rotating linear polarizer was placed before the objective lens (Zeiss, LD Plan-Neofluar, air 63×, NA = 0.75, WD = 1.5 mm) and was rotated at a rate of 10°/s. Each *M* measurement took 36 s.

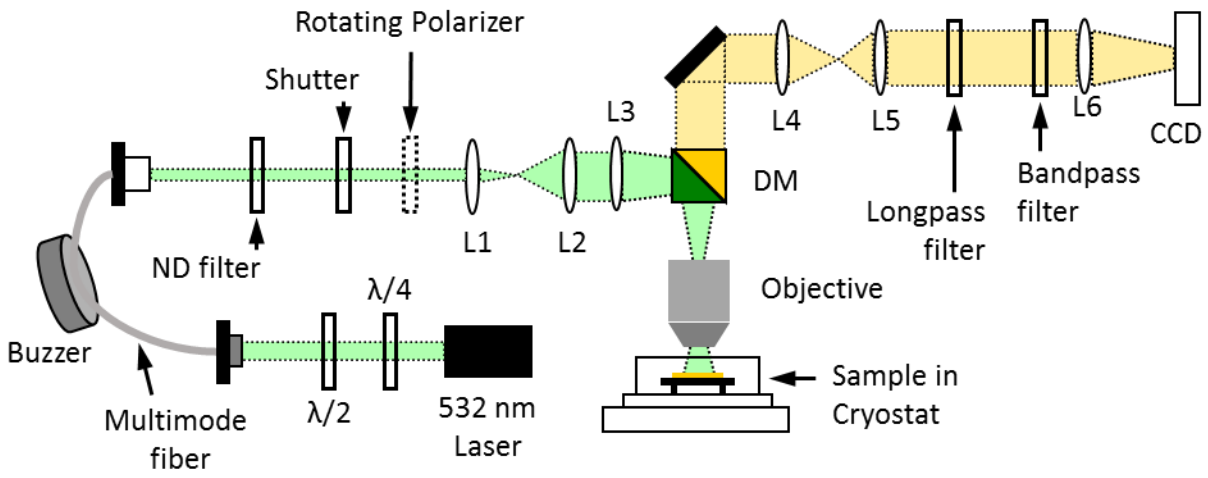

Figure 10. A schematic diagram of the home-built wide-field epifluorescence microscope system used for this experiment. ND stands for neutral density and DM stands for dichroic mirror.

2.2.2 Data Analysis

Collected movies were analyzed using a custom-made program in Python. Feature finding was done using the Crocker-Grier algorithm via Trackpy Python package.[119] Features were excluded from *M* analysis if they exhibited significant photoblinking during a given *M* measurement or showed altered PL intensity at 50 W/cm^2 before and after high intensity measurements. Feature intensity was defined as the mean value of the five brightest pixels of 49 pixels (7 × 7) around each identified feature. Background intensity was obtained in the same way, considering the 32 pixels in the 9 × 9 area that are not a part of the 7 × 7 feature area. To assure statistically equivalent consideration for background and feature calculation, an additional 17 pixels adjacent to the 9 × 9 area were used to provide 49 pixels for the background intensity calculation. Background subtracted frame-by-frame (angle-by-angle) center feature intensity trajectories were used to determine *M* values by fitting the data to Eq 3, with a home-written Python program.

2.3 Results and Discussion

First, circularly polarized excitation light was used to measure PL intensity of a set of single MEH-PPV molecules as a function of excitation intensity from 20 to 200 W/cm^2, which is within the range of typical single-molecule experiments (Figure 11a). The results indicate that significant PL quenching occurs at high excitation intensities, consistent with previous work.[113] However, we also note that there is significant molecule-to-molecule variation in the quenching curves, which is evident in the error bars that represent standard deviation of the PL intensities, with particular molecules showing consistent behavior as a function of increasing excitation intensity (Figure 11b). The molecule-to-molecule variations may emerge from differences in quenching as a function of molecular conformation. There may also be (potentially conformation-dependent) photoactivation processes that compete with the quenching processes, as is evident from particular molecules whose PL intensity increases superlinearly with excitation intensity (Figure 11b). Partial photobleaching, which has also been shown to affect measured polarization modulation values,[106] is not at play, as only molecules with the same PL intensity as excitation power was ramped up and then down were analyzed, thus excluding those molecules exhibiting photobleaching during the experiment.

The intensity-dependent quenching shown in Figure 11 suggests that the quenching effects on *M* values described in the Introduction may occur in these molecules. This is supported by polarization modulation measurements at different excitation intensities performed on these same molecules (Figure 12). Some molecules represented in the intensity-dependent measurements (Figure 11a) were excluded from the analysis represented by Figure 12: these molecules exhibited photoblinking and/or complete photobleaching during the polarization modulation measurements. A representative dataset is shown in Figure 12a: for two excitation powers that vary by a factor of

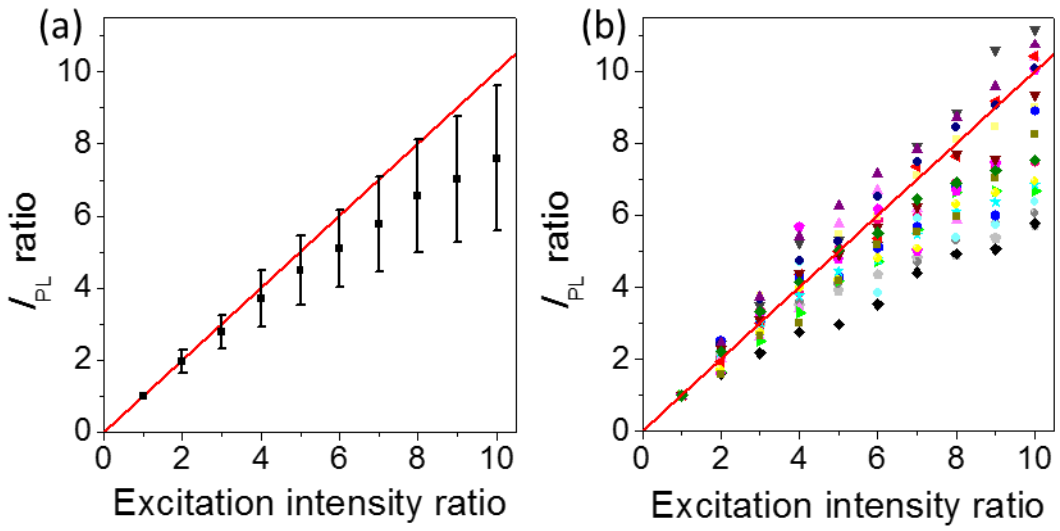

Figure 11. Photoluminescence intensity ratio as a function of excitation intensity ratio for MEH-PPV molecules dissolved in chloroform and immobilized in PS (n = 193). The reference excitation intensity is 20 W/cm^2. Error bars indicate the standard deviations of the PL intensities. (b) Data from 20 single molecules selected at random from the results shown in (a). Red line ($y = x$) is a guide to the eye.

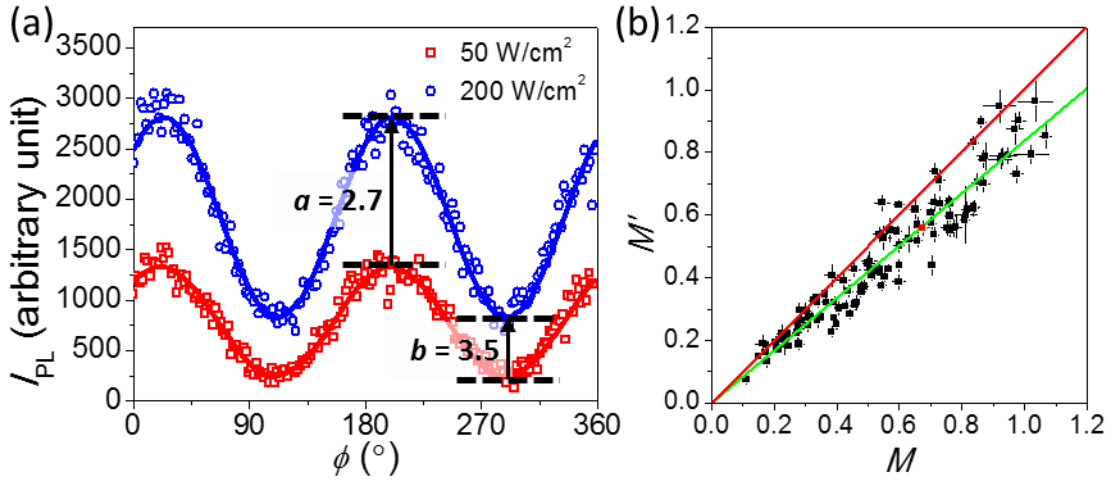

Figure 12. (a) PL intensity as a function of polarization angle of excitation intensity for a single MEH-PPV molecule at 50 W/cm^2 (red) and 200 W/cm^2 (blue). Relative I_{max} (co-efficient a in Eq 7) (2.7) and I_{min} (co-efficient b in Eq 7) (3.5) values are shown. Lines are fits to the raw data (symbols) that are used to obtain the values of M = 0.68 (I_{ex} = 50 W/cm^2) and M' = 0.54 (I_{ex} = 200 W/cm^2) via Eq 3. (b) A scatter plot of M values (measured at I_{ex} = 50 W/cm^2) and M' values (measured at I_{ex} = 200 W/cm^2) for n = 111 molecules. The red point is the molecule shown in (a). Error bars represent fit uncertainty. The red line is a guide to the eye with $y = x$. The green line is a linear fit to the data with slope = 0.84.

4.0, the increase in the ratio of I_{max} (=2.7) is less than that in I_{min} (=3.5). As a result, the measured M value decreases from 0.68 to 0.54. A scatter plot of M and M' values for each MEH-PPV molecule measured at I_{ex} = 50 W/cm^2 (M) and 200 W/cm^2 (M') is shown in Figure 12b. Nearly, all M' values are lower than the M value for the same molecule, with the data well fit by a line with slope of 0.84.

To confirm that photobleaching is not at play and that measurement to measurement variation is not responsible for the observed decrease of M with increasing excitation intensity, M values were measured a second time at 50 W/cm^2 after the high intensity M' measurements were performed. In this case, the best-fit line has a slope of 1.01 (Figure 13), confirming that the tendency toward lower M values at high excitation intensity is not related to photobleaching or noise. To further analyze individual molecules' response, co-efficients a and b as defined in Eq 7 and the ratio a/b are plotted with respect to M values in Figure 14. The data show that higher M molecules have lower a/b ratios, consistent with the greater decrease in polarization modulation as a function of excitation intensity compared to molecules with low M values (Figure 12). Closer inspection of the data shows that $a/b < 1$ for most molecules, as expected. However, the change in the a/b ratio is driven not only by a decrease in a that increases as M increases but also by an increase in b, with many molecules with high M showing b ratios greater than 4, the expected ratio if no quenching was present. Molecules with high M values necessarily have a small value of I_{min}, thus increasing the chance that noise plays a role in changes of this value as a function of conditions.

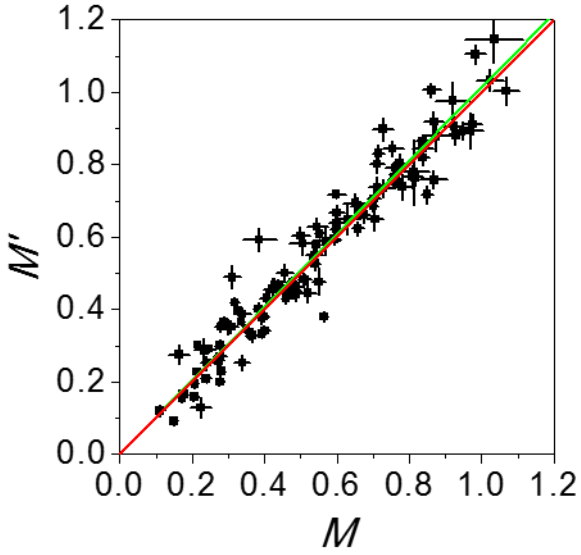

Figure 13. Scatter plot of *M* values of the molecules shown also in Figure 12 measured twice at 50 W/cm^2, before and after the measurement at 200 W/cm^2. Error bars represent fit uncertainty. Red line is a guide to the eye with y = x. Green line is a linear fit to the data with slope = 1.01.

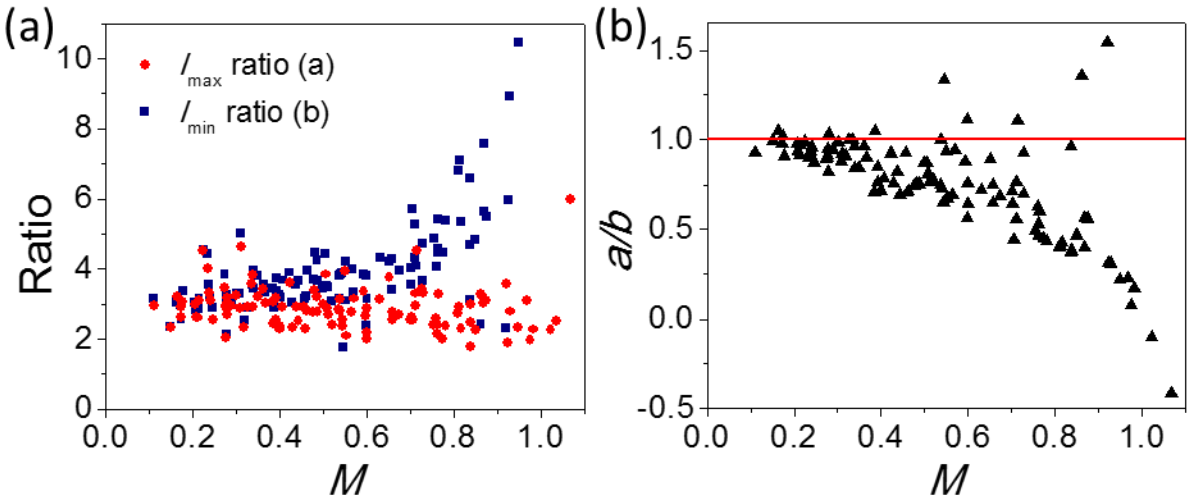

Figure 14. (a) Scatter plots of I_{max} ratio (co-efficient *a* in Eq 7) and I_{min} ratio (co-efficient *b* in Eq 7) vs *M* for the set of molecules also shown in Figure 12. (b) Scatter plot of *a*/*b* vs *M*. Several data points are outside the range shown for *a*/*b*.

To characterize how noise may manifest in these measurements, we performed simulations as detailed in the Appendix B. Briefly, 1000 molecules were simulated to generate an M distribution consistent with the experimental distribution. Following that, both noise and quenching were considered independently for their influence on measured M values as a function of excitation intensity. Figure 15 shows that, as expected, in the absence of noise and any photophysical processes such as exciton–exciton annihilation, measurements of M at two different excitation intensities are identical (Figure 15a,b). The addition of noise affects the results, with the I_{max} ratio (co-efficient a) and I_{min} ratio (co-efficient b) both broadening (Figure 15c). This is more apparent and M dependent for I_{min}, as expected due to the sensitivity of low I_{min} values to noise, which leads to unphysical I_{min} ratios, including negative values and very high positive values of this quantity compared to the expected value of 4. However, in contrast to the experimental data, the spread in I_{max} and I_{min} ratios is rather symmetric, such that the best-fit line for the simulated M' vs M scatter plot retains a best-fit slope of near 1 (slope = 0.99) (Figure 15d).

When exciton quenching is included in the (noise-free) simulation, sublinear changes of I_{min} and I_{max} with excitation intensity are evident (Figure 15e). Beyond that, I_{min} values increase with increasing M, consistent with the experimental data. Incorporating photoinduced quenching according to Eq 4 with $\beta = 2$ best captures the I_{max} suppression seen experimentally. Although this inclusion of quenching also reproduces some aspects of the experimental M' vs M measurements shown in Figure 12, as discussed in the Introduction, intensity-independent M values will be present at 0 and 1 even in the presence of quenching (Figure 15f). Due to the tendency for molecules with high M values to be more strongly affected by noise, adding noise to these simulations including photoquenching recovers the observed behaviors of I_{min}, I_{max}, and M' vs M, with the simulated results showing a slope of 0.84 (Figure 16).

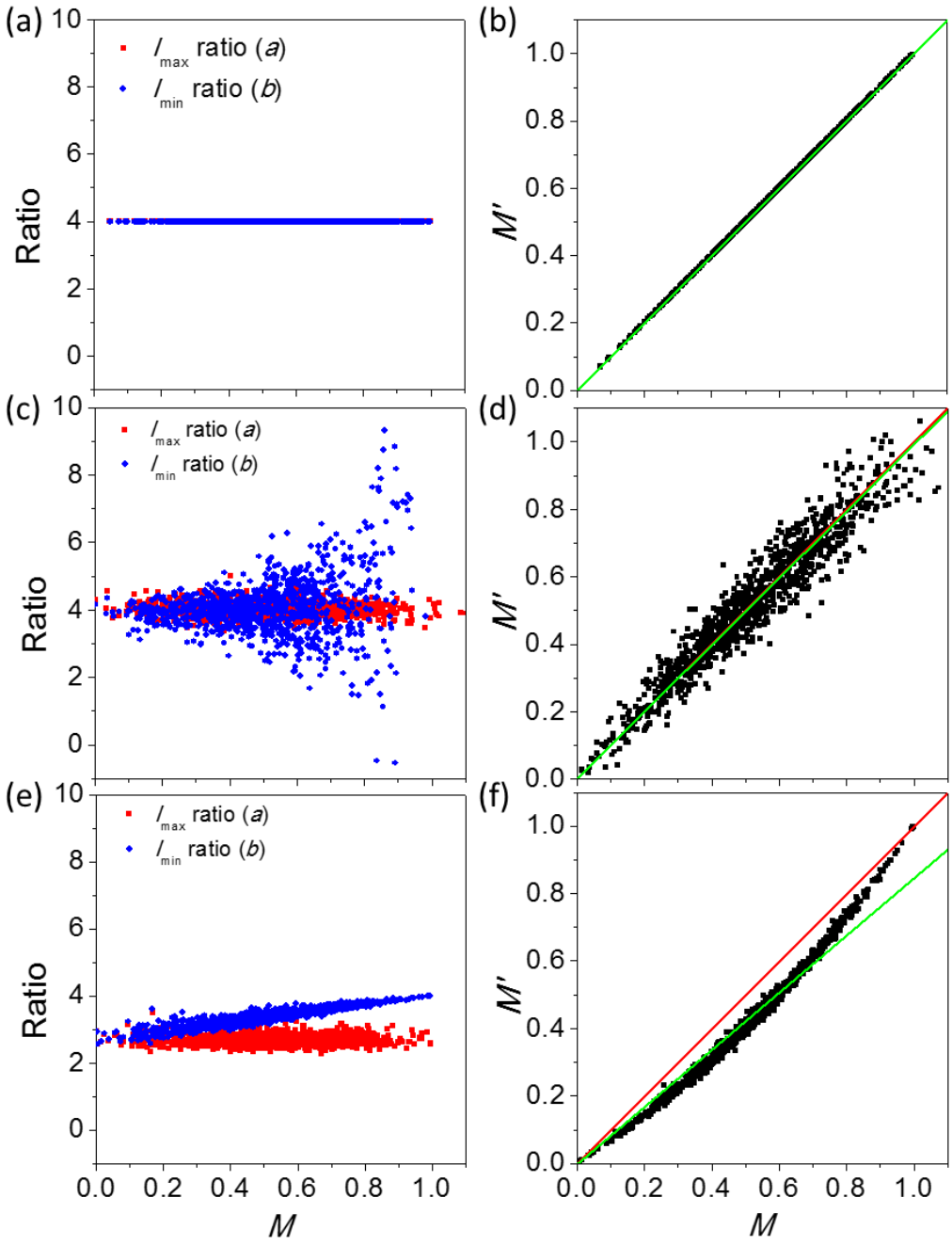

Figure 15. (a) Scatter plots of I_{max} ratio and I_{min} ratio as defined in Eq 7 vs. M for a simulation of 1,000 molecules with neither noise nor quenching and an excitation intensity ratio of 4, as in the experiment. (b) M' vs. M for the simulation also depicted in (a). (c) Scatter plots of I_{max} ratio and I_{min} ratio as defined in Eq 7 vs. M for a simulation of 1,000 molecules with noise as described in the Appendix B but no quenching and an excitation intensity ratio of 4, as in the experiment. (d) M' vs. M for the simulation also depicted in (c). Red line is a guide to the eye, showing $y = x$. Green line is a linear fit to the data with slope = 0.99. (e) Scatter plots of I_{max} ratio and I_{min} ratio as defined in Eq 7 vs. M for a simulation of 1,000 molecules with quenching as described in the Appendix B but no noise and an excitation intensity ratio of 4, as in the experiment. (f) M' vs. M for the simulation also depicted in (e). Red line is a guide to the eye, showing $y = x$. Green line is a linear fit to the data with slope = 0.85.

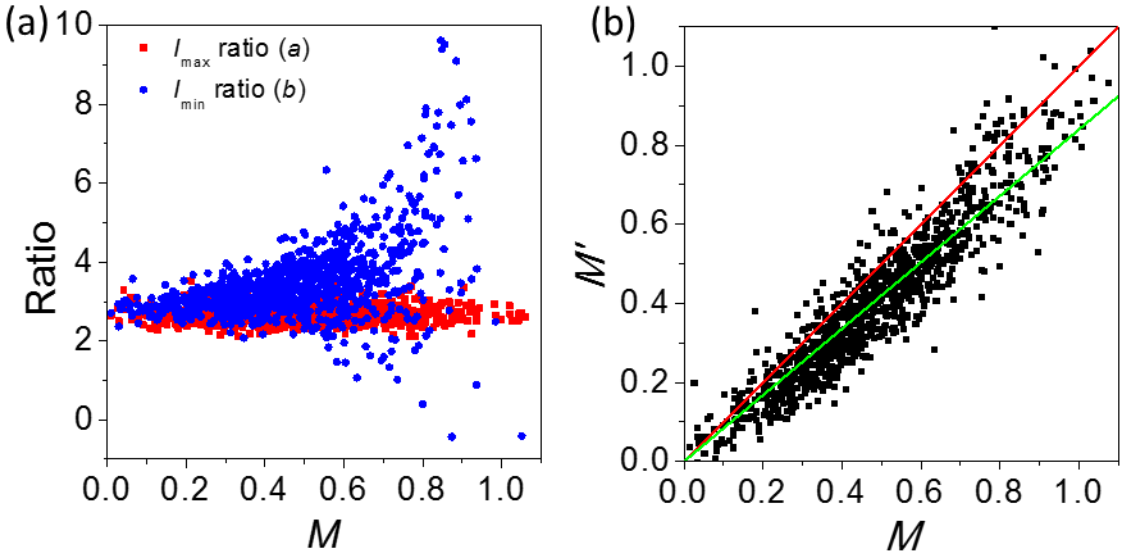

Figure 16. (a) Scatter plots of I_{max} ratio and I_{min} ratio as defined in Eq 7 vs M for a simulation of 1,000 molecules with noise and quenching as described in the Appendix B and an excitation intensity ratio of 4, as in the experiment. (b) M' vs M for the simulation also depicted in (a). The red line is a guide to the eye, showing $y = x$. The green line is a linear fit to the data with slope = 0.84.

Although the measured M suppression at high excitation intensity is consistent with the simulated results, additional photophysics beyond that captured with the quenching described by Eq 4 could also be at play. For example, photoactivation processes are sometimes evident in single-molecule data, with a given molecule becoming brighter over time at a given illumination intensity. Although molecules with strong evidence of such behavior were not present in this dataset (see Figure 13), some do display photoactivation with increasing intensity (Figure 11b). Beyond photoactivation, MEH-PPV displays a broad range of photophysics that may not be captured by Eq 4 and may further be conformation dependent.[47,54,113] Indeed, one may expect the assumption of independent exciton domains to preferentially fail in MEH-PPV molecules with more compact conformation, where efficient exciton funneling exists. Further experimental measurements and theoretical treatment would be needed to clarify these issues; however, our experimental data suggest that MEH-PPV molecules with a range of conformations display photoquenching behavior

and subsequent intensity-dependent *M* values captured by the relatively simple model originally used to characterize intensity-dependent quenching through singlet–triplet annihilation.

2.4 Conclusion

Modulation depth measurements are widely used to determine the degree of anisotropy and conformation of emitting conjugated polymers at the single-molecule and aggregate levels. However, many such materials exhibit complex photophysics, including strong evidence of excitation intensity-dependent photoquenching. We show here that intensity-dependent quenching that manifests in sublinear photoluminescence intensity growth with increasing excitation intensity results in decreasing *M* values as a function of increasing excitation intensity, demonstrating that interpretation of *M* values and changes thereof must be done with caution and should not immediately be attributed to differences in molecular conformation. Beyond the intensity-dependent singlet–triplet annihilation modeled here, other intensity-dependent photophysics may affect measured *M* values, and additional experimental and theoretical work are required to fully clarify origins of intensity-dependent polarization modulation in multichromophoric molecules with complex photophysics such as MEH-PPV.

Chapter 3. Nearly Isotropic Conjugated Polymer Aggregates with Efficient Local Exciton Diffusion

This chapter was reproduced in part from Kwon et al.[120]

3.1 Introduction

Conjugated polymers have been extensively studied over the last two decades due to their potential as functional materials in optoelectronic devices including light-emitting diodes, solar cells, and photovoltaics.[4–9,11,121,122] Attractive qualities of conjugated polymers as components of such devices include their solution processibility, mechanical properties, low production cost, and tunable photophysical properties. However, limitations exist, with conjugated polymer-based devices often suffering from limited device stability and low efficiency compared to their inorganic counterparts.[6,7] Some of these limitations are due to the nature of excitons, the fundamental excitations in conjugated polymers, which are Coulombically bound electron and hole pairs. While exciton migration is key to polymer-based device functionality, exciton migration to extrinsic impurities or intrinsic defects can lead to nonradiative or radiative recombination processes, either or both of which can inhibit desired device function.[1,40,53,123–126] Enhanced understanding and control of exciton behavior can lead to improvement in polymer-based device function, as highlighted by a recent paper in which a conjugated polymer electron donor layer was combined in a double-layered halide architecture.[127] Here, a wide bandgap halide was placed adjacent to a poly(3-hexylthiophene) [P3HT] electron donor layer to limit exciton recombination at the interface; this approach also induced ordered fibrillar morphology in the P3HT that encouraged hole transport, leading to exceptional efficiency for a solar cell employing a conjugated polymer layer.

The presence of multiple chromophores (a base unit for conjugation that consists of several monomers) as may exist on a single conjugated polymer assures complexity in exciton behavior and study thereof.[27,28,35,40,105,128,129] Interactions between chromophores determine the properties of conjugated polymers, including the efficiency and timescale of exciton migration. On a single-chain level, both intrachain (along-chain) and interchain (across-chain) processes can contribute to these properties. In the model conjugated polymer poly[2-methoxy-5-(2-ethylhexyloxy)-1,4-phenylenevinylene] (MEH-PPV), this leads to two distinct behaviors, which are linked to two distinct chain conformations. When dissolved in toluene, regarded as a poor solvent for MEH-PPV, and immobilized in an inert matrix such as poly(methyl methacrylate) or polystyrene, MEH-PPV chains are known to adopt a collapsed and ordered conformation, as supported by evidence of highly aligned transition dipoles in experiments and simulation.[26,33,40,64,68,76,98,130,131] These molecules show stepwise photobleaching and relatively red emission, providing evidence that the chain planarization and/or interchain interactions predominant in MEH-PPV chains with such conformations support relatively long conjugation lengths and facile exciton migration.[40,60,65,72,75,132–134] Alternately, when dissolved in chloroform, MEH-PPV chains adopt a random coil conformation in which intrachain interactions dominate. In this case, the MEH-PPV chains typically show low polarization anisotropy, continuous photobleaching, and higher energy emission.[40,64,65,69,75,106,132,135,136]

Solvent vapor annealing (SVA) technique has been widely used in block copolymer studies to gain control over the polymer ordering in a film, and gained popularity in the conjugated polymer single-molecule studies as well in less than a decade. In single-molecule studies, when exposed to the solvent vapor, the host polymer matrix intakes vapor and swells as a result. In turn, the polymer chains embedded in the matrix gain mobility. Taking advantage of it, Vogelsang *et*

al. demonstrated that the single-chain conformation can be altered using solvent vapor swelling.[64] The authors argued that, since conjugated polymer chains show mobility and their fluorescence intensity increases during the SVA process, the chain must exhibit more open and extended conformation during the solvent exposure, where host polymer matrix must be in the "heterogeneous mixture of solid and liquid-like phase." By measuring the fluorescence polarization modulation depth before and after SVA for MEH-PPV single-molecules, they revealed that regardless of the starting conformation (imposed by the solvent used in the sample preparation), the final confirmation of single-molecules is highly collapsed after SVA.

Though on a single-molecule level the relationship between conformation and photophysical properties has largely been elucidated, the full array of interactions present in densely packed environments such as those in devices cannot be fully recapitulated at the single-molecule level. To enhance understanding of the relationship between conjugated polymer conformation and photophysics, as well as to bridge single-molecule and bulk level studies, aggregates and nanoparticles of conjugated polymers have been the subject of recent work.[76,77,86,87,78–85] It is particularly instructive to study aggregates prepared in a controlled and reproducible manner, and, as such, aggregates have been prepared through solvent vapor swelling , allowing conjugated polymer chains to diffuse and aggregate via Ostwald ripening and/or particle coalescence.[80,83]

Here, we use a multimodal apparatus previously described that affords control over the matrix swelling and conjugated polymer aggregation process and simultaneous wide-field fluorescence imaging[92] characterize single-molecules and aggregates of MEH-PPV in PMMA. First, we focus our attention to the possible conformation change of single-molecules during SVA.

We hypothesize that the solvent used in swelling affects the conformation of the conjugated polymer chain, as the chains can interact with new solvent introduced to the system. To test this theory, the samples were prepared using one of two solvents, toluene and chloroform, each representing a poor solvent and a good solvent. Then, each sample was exposed to the vapor of the same two solvents, resulting in four different combinations. We show that the solvent used during the swelling process does not alter the conformation that was pre-determined by the dissolving solvent. Even though mobile conjugated polymer chains could be observed, and the interaction between solvent and polymer chains is one of the biggest factors in determining conformation, the interaction during the swelling of host matrix is not effective enough for the conformation to change significantly.

In addition to the single-molecule conformation study, MEH-PPV aggregates were also studied. In contrast to our previous work focused on MEH-PPV initially dissolved in toluene,[79] which supports a collapsed and ordered conformation, here we study MEH-PPV initially dissolved in chloroform, which supports the random coil conformation at the single-molecule level. We show that the relatively isotropic conformation of single MEH-PPV chains following dissolution in chloroform is maintained even after multichain aggregation. Previous studies have explored the effects of conjugated polymer conformation at the single-molecule level on aggregate structure and photophysics, but those studies controlled single-molecule conformation by controlling regioregularity or introducing defects or halogen atoms during polymer synthesis.[77,78,84] Here, we show that even a change in dissolving solvent during sample preparation impacts aggregate physical conformation and photophysical behavior despite swelling of the background matrix that allows conjugated polymer mobility. In these systems, we find indications of local enhancement of interchain interactions due to aggregation (red shift of emission spectra and increasing

quenching efficiency) without signs of long-range exciton migration that were apparent in aggregates templated on MEH-PPV molecules with collapsed and ordered conformation.[79] This chapter provides insights into the complex relationship between polymer morphology and energy transfer, adding to the set of findings suggesting the importance of sample preparation in setting exciton migratory capacity in conjugated polymers across scales.[68,77,84,108,137–139]

3.2 Methods

3.2.1 Sample Preparation

For single-molecule conformation study, MEH-PPV (M_n = 160 kDa and PDI = 1.05) was purchased from Polymer Source and was used without further purification. Poly(methyl methacrylate) (PMMA; M_w = 97 kDa and PDI = 2.2) was purchased from Sigma-Aldrich and purified before use.[140] MEH-PPV solutions were prepared by dissolving MEH-PPV in either toluene or chloroform (HPLC plus grade), which were purchased from Sigma-Aldrich and used without further purification. The prepared MEH-PPV solutions were ~ 10^{-11} M, which was furthur mixed with either ~6 wt% PMMA/toluene or ~2.5 wt% PMMA/chloroform solution at a 1:500 ratio to have the final concentration typically used for single molecule studies. Spin-coating was used to deposit the solutions onto piranha-cleaned glass coverslips, which resulted in emissive feature density of ~0.7 spots/μm^3.

For aggregate study, MEH-PPV (M_w = 168 kDa and PDI = 2.1) was synthesized as described previously.[141] MEH-PPV solutions of four different concentrations—concentrations A, B, C, and D—were prepared by dissolving MEH-PPV in chloroform. Concentration A was ~ 10^{-11} M and concentrations B, C, and D were 10, 100, and 1000 times concentration A, respectively. The prepared MEH-PPV solutions were then mixed with ~ 2.5 wt% PMMA/chloroform solution

as described above. Spin-coating was used to deposit the solutions onto piranha-cleaned glass coverslips, which resulted in emissive feature density of ~0.4 spots/μm^3 for concentration A.

3.2.2 Solvent Vapor Annealing (SVA)

The SVA technique employed is described in detail in Appendix A and our previous publication.[92] Briefly, a solvent reservoir, a mixing bottle, and three mass flow controllers (MFCs; Alicat Scientific, two MCS-100SCCMs and one MCS-200SCCM) were used to control the solvent vapor flow of the system. First, dry N_2 gas was introduced to the solvent reservoir through an MFC where the flow rate was controlled. The solvent vapor was generated by bubbling the N_2 gas in the solvent reservoir. For single-molecule conformation study, either toluene or chloroform was used as a single source of solvent vapor. For aggregation, a mixture of chloroform and acetone (50:50 liquid volume ratio; 43.7:56.3 vapor ratio) was used. The solvent vapor entered the mixing bottle, where more N_2 gas could be introduced through two additional MFCs if needed. The solvent vapor then traveled to the SVA chamber where two films were placed, one deposited on a glass coverslip, used for wide-field fluorescence measurements, and one on a quartz crystal microbalance (QCM) sensor, used for monitoring the SVA process. The QCM (Stanford Research Systems, QCM-200) detected mass change of the film, which was converted to changes in film thickness. For single-molecule conformation study, the initial thickness of sample films was 300 ± 10 nm, and during SVA, the swollen film thickness varied, which will be specified in the results section. For aggregate study, the initial thickness of sample films was 210 ± 5 nm, and during SVA, unless otherwise specified, the swollen film thickness was 535 ± 5 nm, which was controlled through N_2 flow into the solvent reservoir that in turn controls the solvent vapor flow rate, adjusting the MFC as needed for the duration of swelling. Except when otherwise noted, films were swollen for 50

min and then deswelled by flowing dry N_2 gas into the SVA chamber. All experiments were carried out at room temperature (21 °C).

3.2.3 Wide-Field Epifluorescence Imaging

A home-built wide-field epifluorescence microscope system (Figure 17), different from the one used in Chapter 2, was used to perform the experiments. A continuous-wave 488 nm diode laser (Thorlabs, L488P60) was used as the excitation source. It was coupled to a multimode fiber that was mechanically shaken to improve homogeneity of the illumination. A linear polarizer and a quarter-wave plate were used to generate circularly polarized light. The beam then passed through a laser line filter and a collimating lens, reflected off a dichroic mirror, and was focused onto the back-focal plane of an oil-immersion objective (Olympus PlanApo N 60×, NA = 1.45). For polarization modulation measurements, a motorized rotating linear polarizer was placed before the dichroic mirror and rotated at 10 °/sec. The fluorescence from the sample was collected with the same objective and was filtered using a 514 nm long-pass filter before imaging onto an EMCCD camera (Andor, iXon DV885 KCS-VP). The 14-bit images were recorded over 512 pixels × 512 pixels. The final field of view was 47 μm × 47 μm.

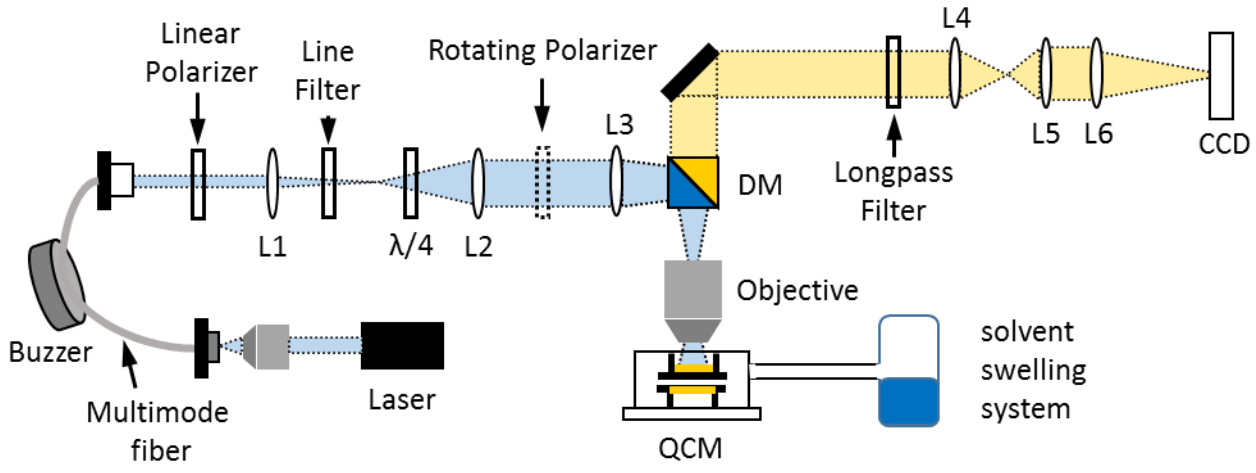

Figure 17. A schematic diagram of the home-built wide-field epifluorescence microscope system used for this experiment.

3.2.4 Data Analysis

All fluorescent features were first identified using the Crocker-Grier algorithm via the Trackpy Python toolkit.[119] The intensities of identified features were then calculated and background-corrected using a custom program written in Python. For single-molecule conformation study, the mean value of the five brightest pixel in the area of 9 × 9 around identified feature was used as fluorescence intensity. Other details such as background subtraction are the same as in Chapter 2.

Alternatively, for aggregate study, fluorescence intensity, I_{AGG}, was calculated by subtracting the contribution from the background single MEH-PPV chains as well as camera noise:

$$I_{AGG}(or\ I_{SM}) = \sum_{X=1}^{N}\sum_{Y=1}^{N} I_{P,XY} - N^2 I_{P,film-median} \qquad \text{Eq 8}$$

N is the number of pixels over which the feature size is defined, $I_{P,XY}$ is pixel intensity within the feature, and $I_{P,film\text{-}median}$ is the median pixel intensity of the field of view, which represents the sum of signal from the remaining dispersed MEH-PPV single-chains and camera noise. For these calculations, we chose N = 13. The fluorescence intensity of single MEH-PPV chains, I_{SM}, which is relevant for films of concentration A before and after SVA, is also calculated via the above equation, and here $I_{P,film\text{-}median}$ is due only to camera noise.

3.2.5 Spectroscopy Setup and Spectral Data Analysis

To collect photoluminescence spectra, a spectrograph (Andor Shamrock 193i) was placed before the EMCCD camera. When collecting spectra, a 498 nm long-pass filter was used in place of the 514 nm filter and the 14-bit images were recorded over 1002 × 1004 pixels. All spectra were fit to three Gaussian or Voigt functions via least-squares fitting except as noted. Peak positions

and relative heights were determined from the sum of the deconvolved spectra, which is the reconstructed spectrum without noise, except where noted.

3.3 Results and Discussion

3.3.1 Single-Molecule Conformation Study

To compare conformation of MEH-PPV single-molecules, polarization modulation depth (*M*) measurements were performed before and after SVA. *M* was obtained by rotating a linear polarizer while collecting fluorescence images. Fluorescence intensities of MEH-PPV molecules were plotted as a function of polarization angle and fit to the function $I(\phi) = I_0[1 + Mcos\{2(\phi - \phi_0)\}]$, where ϕ is polarization angle, ϕ_0 is a reference polarization angle at the intensity maximum, and I_0 is a reference fluorescence intensity at the intensity maximum. *M* values report the alignment of absorbing transition dipoles and thus report on the conformation of MEH-PPV molecules or aggregates, with *M* near 1 for molecules or aggregates with highly aligned chromophores and close to 0 for isotropic chromophore arrangement.

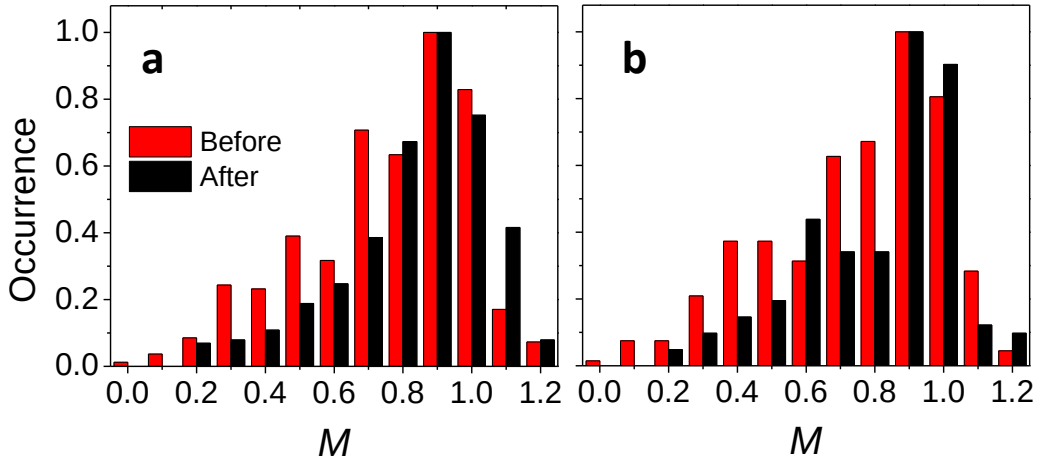

Figure 18. *M* histograms of MEH-PPV single-molecules prepared in toluene, before (red) and after (black) SVA. Each sample was swollen using (a) toluene and (b) chloroform during SVA. The films were swollen for 60 min, and swollen film thicknesses were (a) 385 ± 10 nm and (b) 445 ± 10 nm. Total number of features represented by the histograms are (a) 390 and 409, and (b) 326 and 153 for before and after SVA, respectively.

For MEH-PPV single-molecules initially dissolved in toluene, the histograms of the *M* values measured before SVA show median values of 0.86 and 0.85, shown in Figure 18a and b, in close agreement with literature.[64,76,79,130] When SVA was performed on the samples using two different solvents, toluene (Figure 18a) and chloroform (Figure 18b), the measured *M* values after SVA both showed medians of 0.94, only a slight shift from the median values before SVA. This indicates that regardless of the solvent used for swelling, SVA induces only a small degree of conformation change in MEH-PPV single-molecules prepared in toluene. Especially notable is that even when the molecules were exposed to chloroform during SVA, which is a good solvent that dissolves MEH-PPV better and promotes more open conformation, the MEH-PPV single-molecule conformation stays in its original ordered-collapsed state.

When *M* measurements were performed in MEH-PPV single-molecules initially dissolved in chloroform instead of toluene, the histograms of single-molecule *M* values before SVA show the median *M* values of 0.72, again in close agreement with literature (Figure 19).[64] Similar to the results shown above, after SVA with two different solvents, toluene (Figure 19a) and chloroform (Figure 19b), the median *M* values show only a small change to 0.68 and 0.79, respectively, contradicting the previously reported results.[64]

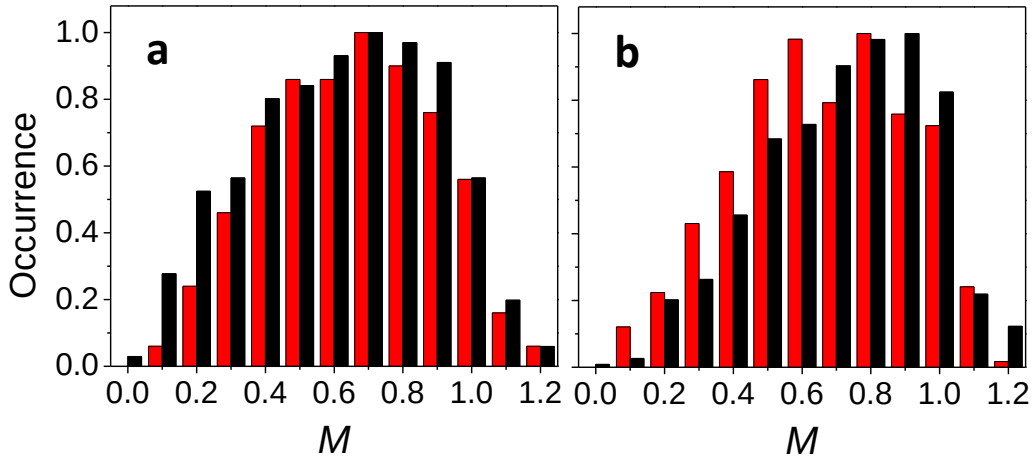

Figure 19. *M* histograms of MEH-PPV single-molecules prepared in chloroform, before (red) and after (black) SVA. The solvent used for swelling was (a) toluene and (b) chloroform. The films were swollen for 120 min, and swollen film thicknesses were (a) 410 ± 10 nm and (b) 585 ± 10 nm. Total number of features represented by the histograms are (a) 332 and 776, and (b) 393 and 734 for before and after SVA, respectively.

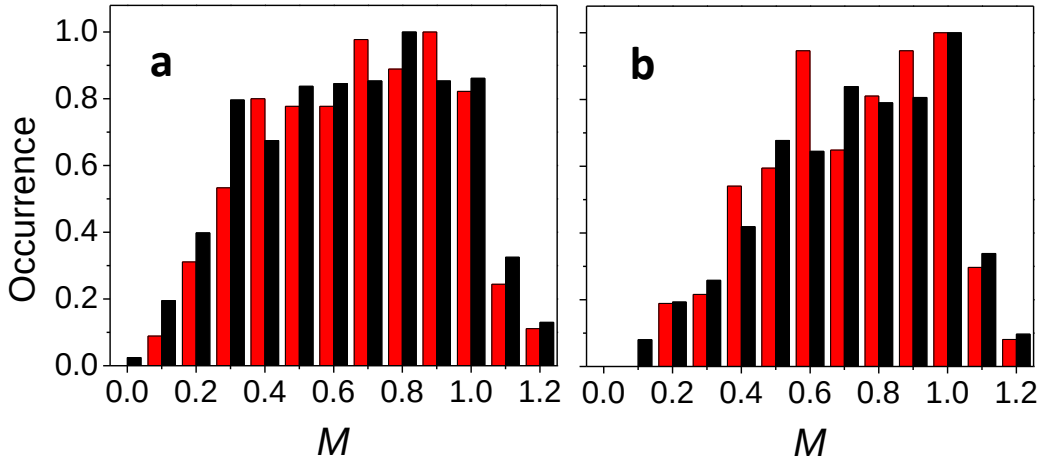

Figure 20. *M* histograms of MEH-PPV single-molecules prepared in chloroform, before (red) and after (black) SVA. The solvent used for swelling was (a) toluene and (b) chloroform. The films were swollen for (a) 70 min and (b) 30 min, and swollen film thicknesses were (a) varied from 445 ± 10 nm to 525 ± 10 nm and (b) 865 ± 10 nm, respectively. Total number of features represented by the histograms are (a) 333 and 962, and (b) 236 and 386 for before and after SVA, respectively.

To eliminate the possibility that the swelling of films was insufficient, SVA was repeated using the same two solvents with higher degrees of swelling. The initial median *M* values before SVA were 0.74 and 0.81 for the histograms shown in Figure 20a and b, and the medians barely change after SVA, showing values of 0.71 and 0.8. Despite the fact that this sample was sufficiently swollen to allow obvious molecular mobility, the single molecules apparently adopted similar conformations after SVA as that displayed following initial sample preparation through spin-coating. This stands in contrast to a previous study in which MEH-PPV was dissolved in chloroform and swollen in toluene vapor, in which the *M* values shifted to higher values signaling molecular collapse and ordering.[64]

3.3.2 Aggregate Study

Wide-field fluorescence images were collected before and after SVA for sample films of concentrations A–D (Figure 21). In films of concentrations A and B, individual bright features on a dark background are evident before SVA and the number of such features decreases after SVA, with this change quite subtle in films of concentration A and quite obvious in films of concentration B. For films of concentrations C and D, a bright background exists due to the large number of single molecules present that result in overlapping imaged features. In these samples, fluorescence intensity of the background of the films decreases significantly after SVA and the intensity of the clearly identifiable features increases. Taken together, this suggests that in samples B–D, single molecules aggregate to form multichain entities as a result of SVA. From here forward, we denote these features as aggregates B–D. Figure 22 shows the fluorescence intensity histograms of identified features of sample films before and after SVA for concentration A and after SVA for concentrations B–D. Fluorescence intensity of bright features following SVA increases as a

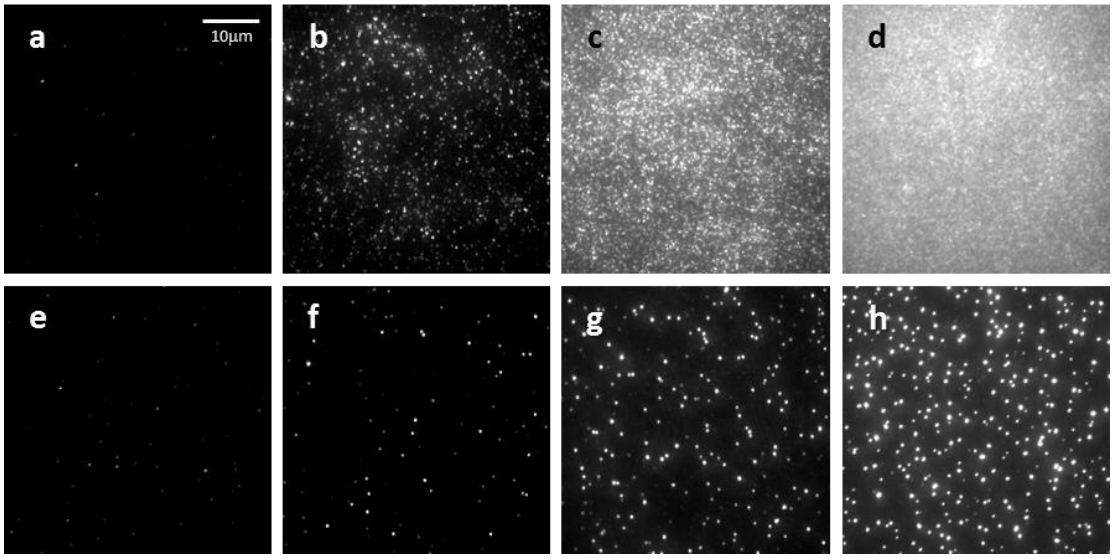

Figure 21. Representative wide-field fluorescence images of films of concentrations A–D (a–d) before and (e–h) after SVA. Intensity scale for the images is 1100–1500, 1100–2550, and 1100–10000 counts per 200 ms for films of concentrations A and B, C, and D, respectively. Excitation power density was 2.5 W/cm^2 for all films.

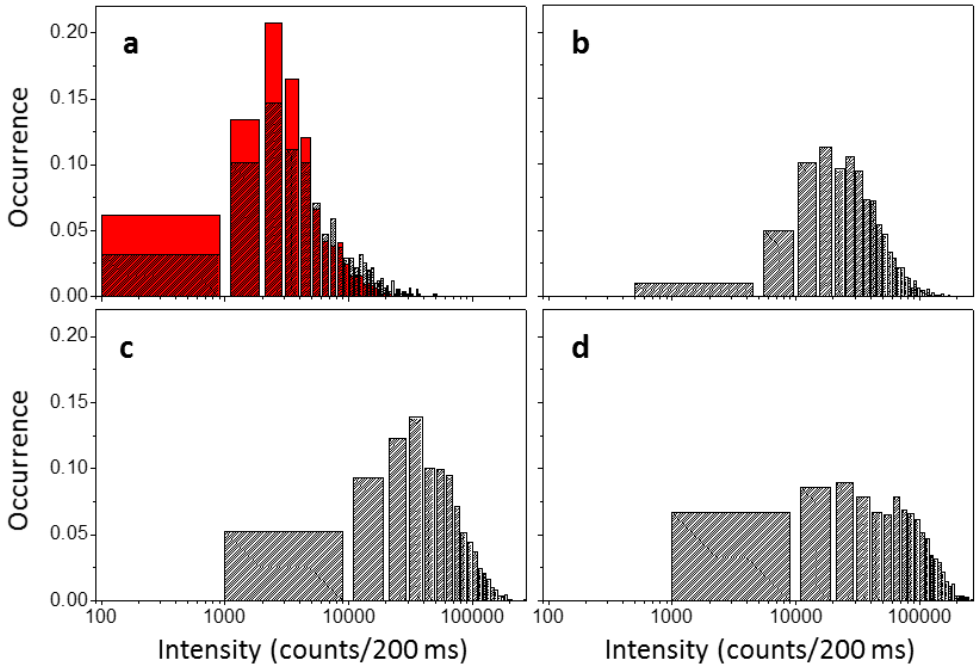

Figure 22. Histograms of fluorescence intensity of identified features in (a) concentration A (red) before and (black) after SVA and (b–d) concentrations B–D after SVA. The median intensities are 3500, 5090, 31500, 49200, and 66000 counts per 200 ms at 5 W/cm^2, respectively. Measurements were taken over at least 5 fields and total number of features represented by the histograms are 890, 591, 1692, 1621, and 1108 for films of concentration A before SVA and after SVA and for films of concentrations B–D after SVA, respectively. Histograms are normalized by total area.

function of initial MEH-PPV concentration, suggesting that at higher initial concentrations, larger aggregates are formed.

For aggregate study *M* measurements to assess conformation, excitation power densities were 7.5, 1.0, 0.5, and 0.5 W/cm^2 for concentration A before and after SVA, and concentrations B, C, and D after SVA, respectively. This power is low enough to avoid potential *M* value suppression due to exciton-exciton annihilation[93,113] as well as to suppress potential variation in signal from MEH-PPV molecules remaining in the background.[79]

The histogram of single-molecule *M* values before SVA shown in Figure 23a shows a median value of 0.66, in close agreement with previous results for MEH-PPV single molecules initially dissolved in chloroform.[64] We note that sample A shows little change in median *M* value after SVA (median *M* = 0.64). The same as the single-molecule conformation study results, here, in spite of adequate swelling of the sample, the single-molecules maintained their conformations regardless of SVA. In the current work, swelling was performed in a combination of chloroform and acetone, and while acetone has been reasoned to be a poor solvent for MEH-PPV owing to its high polarity, in combination with chloroform it apparently does not induce the collapsed, ordered conformation. Given the consistency of *M* measurements before and after SVA for films of concentration A, presumably the template for aggregate formation is a poorly ordered, loosely arranged MEH-PPV molecule. This is consistent with findings for polarization modulation values in aggregates B–D. Aggregates B show little shift from the single-molecule *M* distribution, while for the larger aggregates, decrease in *M* values is apparent, with median values decreasing from the single-molecule value of 0.66 to 0.37 and 0.16 for aggregates C and D, respectively. This is in contrast to large aggregates initially templated on the collapsed, ordered single molecules prepared in toluene, where aggregates with several hundred molecules showed *M* distributions peaked above

0.60.[79] While the *M* distributions of the aggregates prepared in this study are indicative of largely isotropic aggregates, we note that these values are still higher than would be expected from large aggregates with fully randomized transition dipole orientation.[106]

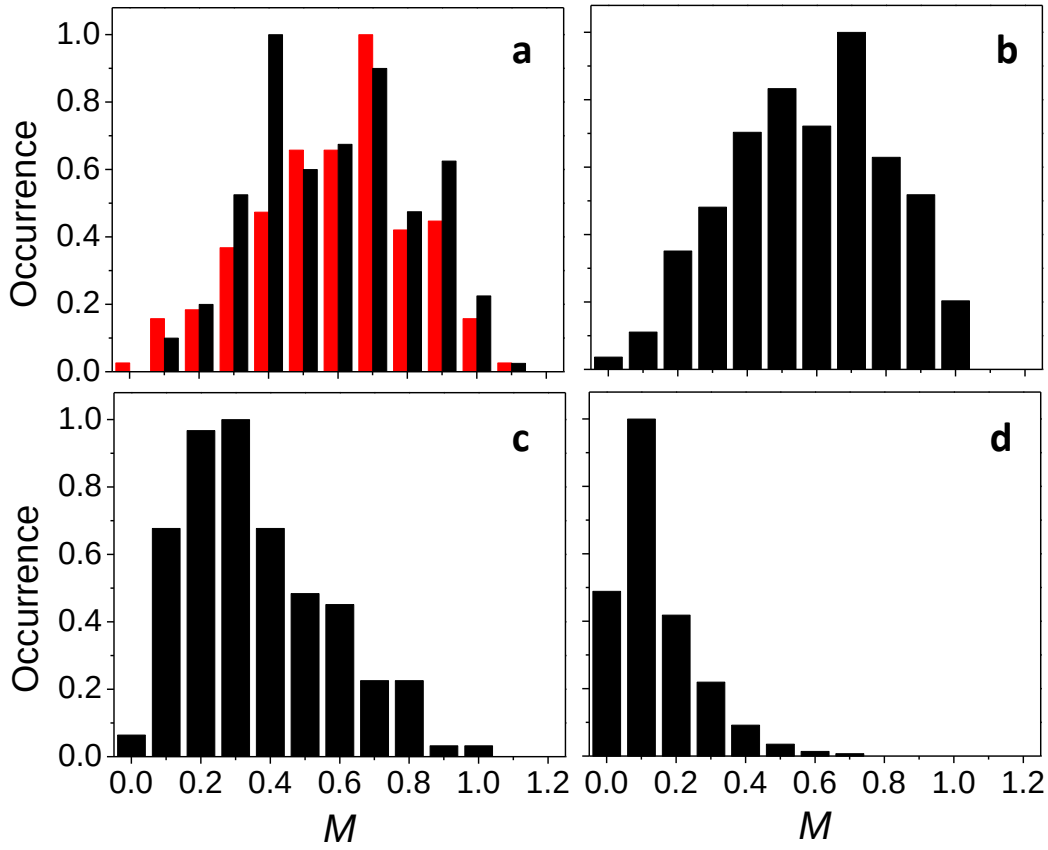

Figure 23. Histograms of polarization modulation depth (*M*) of features identified in (a) films of concentration A (red) before and (black) after SVA and (b–d) films of concentration B–D after SVA. The median *M* values are 0.66, 0.64, 0.63, 0.37, and 0.16, respectively, for concentration A before and after SVA and aggregates B–D. Measurements are taken over at least 3 fields and total number of features represented by the histograms are 174, 214, 302, 150, and 321 for films of concentration A before SVA and after SVA as well as for films of concentrations B–D after SVA, respectively.

To characterize additional aspects of the photophysical behavior of MEH-PPV aggregates, fluorescence intensity transients were collected, with representative plots shown in Figure 24. To encourage photobleaching, the transients were collected using a high excitation power density of 200 W/cm^2. Some intensity transients in samples of concentration A before and after SVA show

stepwise photobleaching, but many show relatively smooth decays, as shown in Figure 24a and consistent with previous measurements of MEH-PPV single molecules dissolved in chloroform, and with the latter behavior associated with intramolecular exciton transport interrupted by many recombination events.[65,75,132] The lack of distinct photoblinking and photobleaching events is also seen in aggregates B–D (Figure 24b–d). This behavior is again in contrast to MEH-PPV aggregates formed from molecules initially dissolved in toluene, where distinct steps in fluorescence transients were apparent in aggregates comprised of up to several hundred MEH-PPV chains.[79]

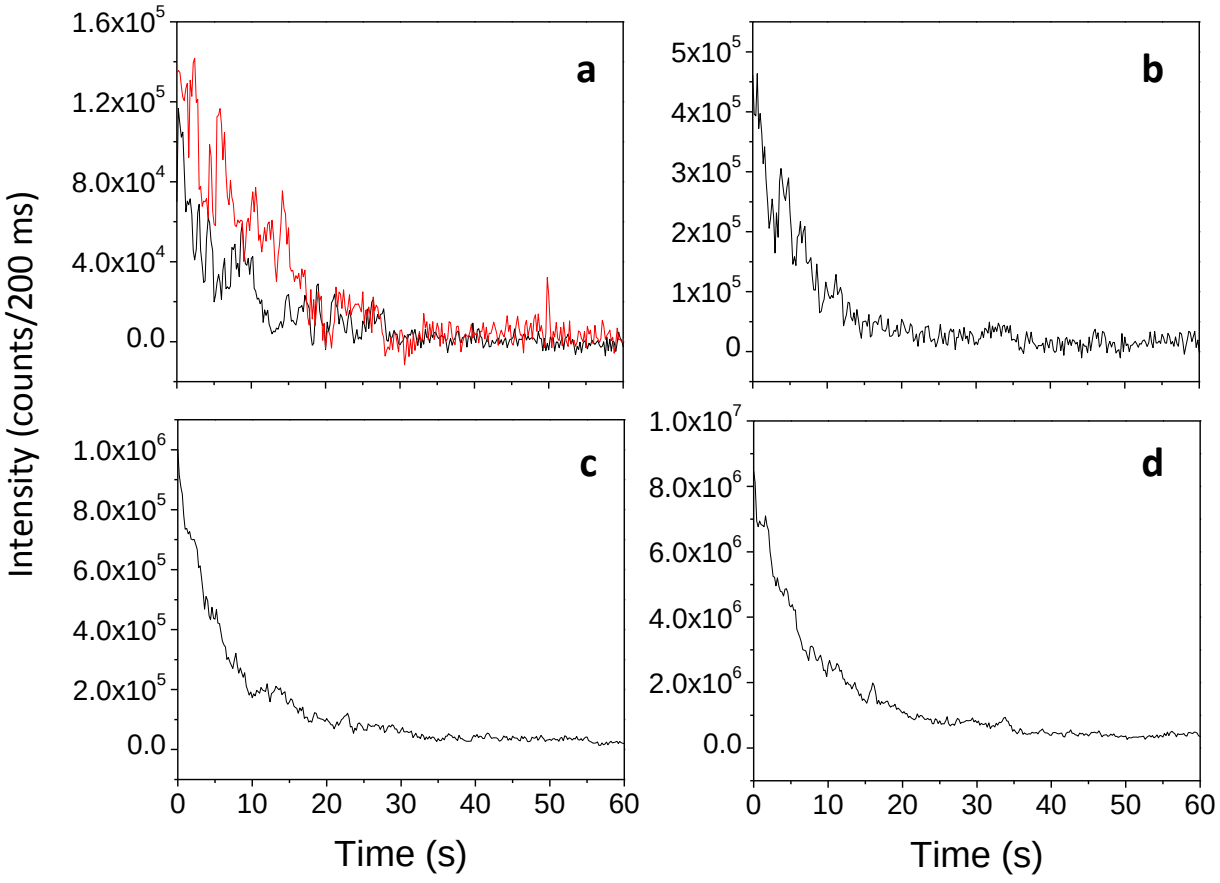

Figure 24. Representative fluorescence intensity transients of features found in (a) films of concentration A (red) before and (black) after SVA and (b–d) aggregates B–D.

To further characterize the photophysics of the MEH-PPV aggregates, photoluminescence spectra were collected. In Figure 25a, representative individual and average spectra of single molecules of MEH-PPV dissolved in chloroform and dispersed in PMMA before SVA are shown. As described previously for molecules of similar molecular weight following dissolution in chloroform and immobilization in a polymer matrix, the individual spectra are generally broad, with many molecules showing a 0-0 peak near 545 nm and a second peak near 580 nm.[65] A few molecules display a somewhat red shifted spectrum, with 0-0 peak near 570 nm. Spectra of the features found following SVA are distinct from those before SVA, with increased homogeneity across features and somewhat narrower spectral bands (Figure 25b). These features have notably red-shifted spectra relative to features found before SVA, with the median peak position of the 0-0 and 0-1 peaks at ~570 (Figure 25c) and 625 nm, respectively. Such spectra have previously been associated with relatively large MEH-PPV molecules exhibiting collapsed conformations[48,65,67,142–144] as well as with tightly packed aggregates[81,84,145,146]; in both cases, chain planarization, π-π stacking, and extension of effective conjugation length can occur, potentially allowing excitons to efficiently funnel to red sites through interchain or intermolecular contacts. In particular, the shifts seen between spectra obtained from films of concentration A before and after SVA are quite similar to those seen previously when single molecules of MEH-PPV were dissolved in tetrahydrofuran (THF), a good solvent for MEH-PPV, and interrogated first at the single-molecule level and then following aggregation to 10–100 nm nanoparticles formed via re-precipitation through rapid addition of water to MEH-PPV in THF solution.[81]

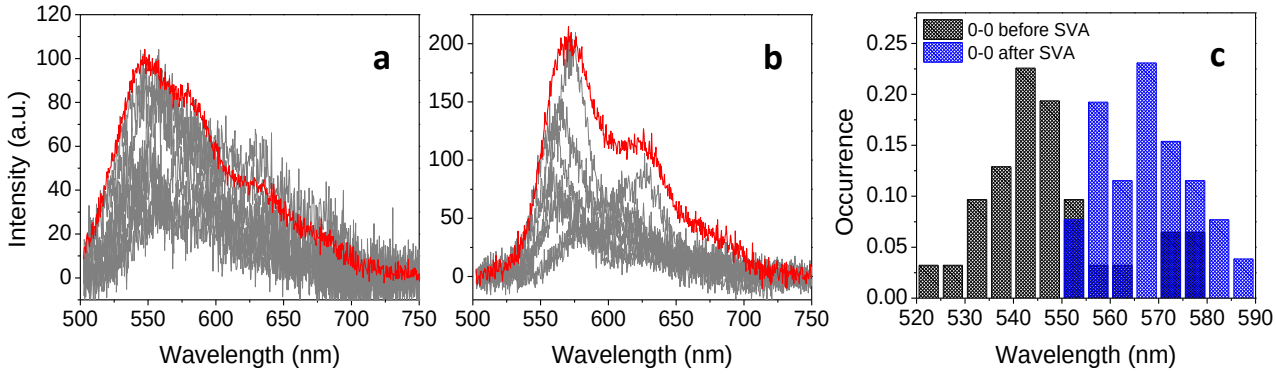

Figure 25. (a,b) Eight representative (grey) individual spectra and (red) the average spectrum of MEH-PPV features found in films of concentration A (a) before and (b) after SVA. Average spectra are obtained from 23 and 26 individual spectra before and after SVA, respectively. (c) Histograms of 0-0 peak positions of MEH-PPV features before and after SVA.

While such a shift towards lower energy emission is consistent with aggregation, it is also consistent with molecular collapse. While no shift in the distribution of *M* values before and after SVA in films of concentration A that would point to collapse was apparent, to clarify whether the spectral shift was due to conformational change or to the formation of small aggregates, samples of concentration A were prepared and subjected to a degree and time of swelling expected to allow for conformational change but that did not result in obvious translational diffusion. For this experiment, 10 min of SVA was performed using the same mixture of chloroform and acetone used in all other measurements. Swelling was held to approximately one-third of that of the typical experiments, with average swollen film thickness of ~300 nm vs. 535 nm. This experiment showed no change in spectra before and after SVA (Figure 26). This supports the idea that the spectral change observed in films of concentration A before and after SVA is not due to conformational change in the single molecules but instead to aggregation.

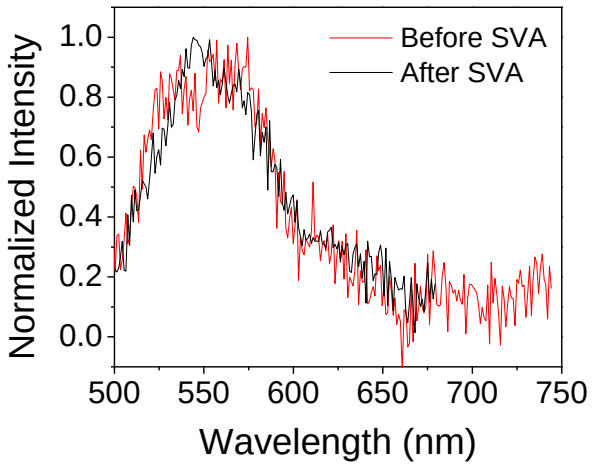

Figure 26. Average spectra of features identified in films of concentration A (red) before and (black) after SVA with swelling performed to a lesser degree and for a shorter time than in other measurements, as described in the text. These spectra were collected using a transmission grating in front of a CCD camera rather than on a spectrograph as described in the Methods section. Spectra were averaged over 10 and 15 individual features before and after SVA, respectively, and the excitation power density was 300 W/cm^2.

For films of concentration A, features are well separated and distinct both before and after SVA and the background level between those features is consistent with that of the pure host polymer matrix alone. As such, feature-finding is an appropriate way to characterize number of molecules per aggregate following SVA. Over five fields of view, before SVA, 233 ± 50 features, assumed to be single molecules, as supported by the spectra, were found; after SVA, 149 ± 9 features were found. This suggests approximately two molecules are present per feature following solvent vapor annealing. Interestingly, the increase in homogeneity and red shift seen before and after SVA occurs even with this very small degree of aggregation. We next investigated the spectra of aggregates formed following SVA of films of concentrations B–D. Peak positions in the aggregates shift to the red with increasing size, with 0-0 and 0-1 peak positions shifting from 572 to 584 and from 623 to 635 for aggregates A–D, respectively (Figure 27). The relative height of the 0-0 and 0-1 peaks also evolves from aggregates A through D, decreasing as a function of aggregate size (Figure 27b).

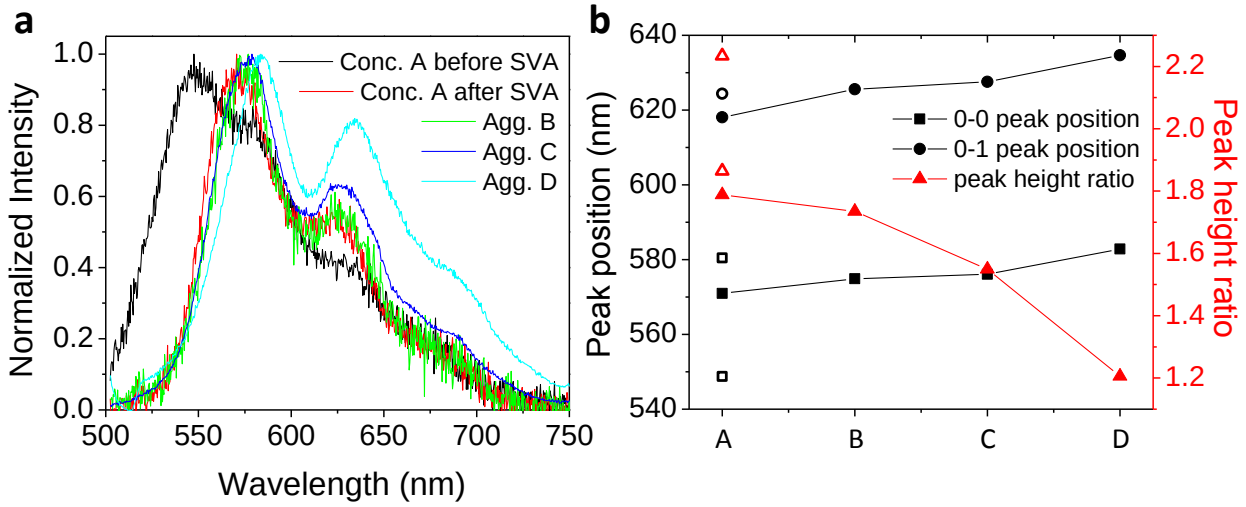

Figure 27. (a) Ensemble-averaged spectra of MEH-PPV in films of concentration A before and after solvent vapor annealing as well as of aggregates B–D. The excitation power densities used were 280, 280, 330, and 88.7 W/cm^2, for films of concentrations A–D, respectively. Spectra for concentration A are also shown in Figure 25a. Number of individual spectra averaged for aggregates B–D are 9, 12, and 7, respectively. (b) (Black squares) 0-0 peak position, (black circles) 0-1 peak position, and (red triangles) 0-0/0-1 peak height ratios for features in films of concentration A–D as obtained from average spectra shown in (a). The results for concentration A before SVA are shown as open symbols. This spectrum was fit with four Gaussian functions: the two squares show the positions of the first two peaks and the open circle indicates the position of the third peak. Peak ratios between the first and third and the second and third peaks are shown as open triangles.

The changes in aggregate spectra as a function of initial film concentration prompted analysis of number of molecules per aggregate, $N_{SM\text{-}AGG}$. While this quantity in films of concentration A was assessed using a feature-finding approach as described above, to characterize aggregate size in films of higher concentrations, we used an approach similar to one we devised previously[79] and is described in Appendix C: this approach (1) does not require that all features be identified and counted before SVA, as becomes increasingly difficult at high initial film concentration and (2) does not assume aggregate intensity reports directly on number of single chains in aggregates, since quenching phenomena are known to occur upon aggregation.[85] Instead, this approach uses background film intensity after SVA to characterize the number of molecules remaining in the background and the number of aggregates present after SVA to calculate the number of molecules present, on average, in each aggregate. This approach assumes intensity

emerging from the background of the samples is due to single-molecule emission. However, spectra obtained from the background of such samples following SVA suggested this was not a good assumption for films of concentration C and D, as here spectra from the film in locations with no obvious aggregates following SVA showed spectral features consistent with aggregates rather than single molecules (Figure 28). With this in mind, the number of single molecules per aggregate, $N_{SM\text{-}AGG}$, was calculated, yielding $N_{SM\text{-}AGG} = 30 \pm 5$, 255 ± 11, and 1640 ± 69 molecules per aggregate for aggregates B–D, respectively. Comparing the number of molecules per aggregate with the intensities per aggregate (Figure 21), it is clear that intensity does not scale linearly with number of molecules and quenching is strong in the aggregates formed here, with quenching efficiency increasing with aggregate size, the same trend that was found in the toluene-prepared aggregates in our previous publication.[84]

Taking together information obtained from *M* measurements, intensity transients, and spectra both in single MEH-PPV molecules and aggregates, a seeming juxtaposition emerges. *M* distributions show relatively low anisotropy both at the single molecule and aggregate level, with aggregates of increasing size showing strongly decreasing median *M* values, especially compared to aggregates formed in toluene.[79] This suggests aggregation is occurring not in a manner that leads to compaction and ordering but instead in a manner that inhibits formation of a large number of new intermolecular contacts that support exciton funneling to low-energy sites. This is consistent with smoothly decreasing intensity transients that point to interruption of such potential exciton funneling with large numbers of (relatively low-intensity) radiative events. In contrast, a strong red spectral shift is seen following SVA, suggesting that exciton funneling to low-energy sites is occurring. The fact that such a spectral shift happens already upon aggregation of just a few molecules (aggregate A) with little additional spectral peak position evolution upon further

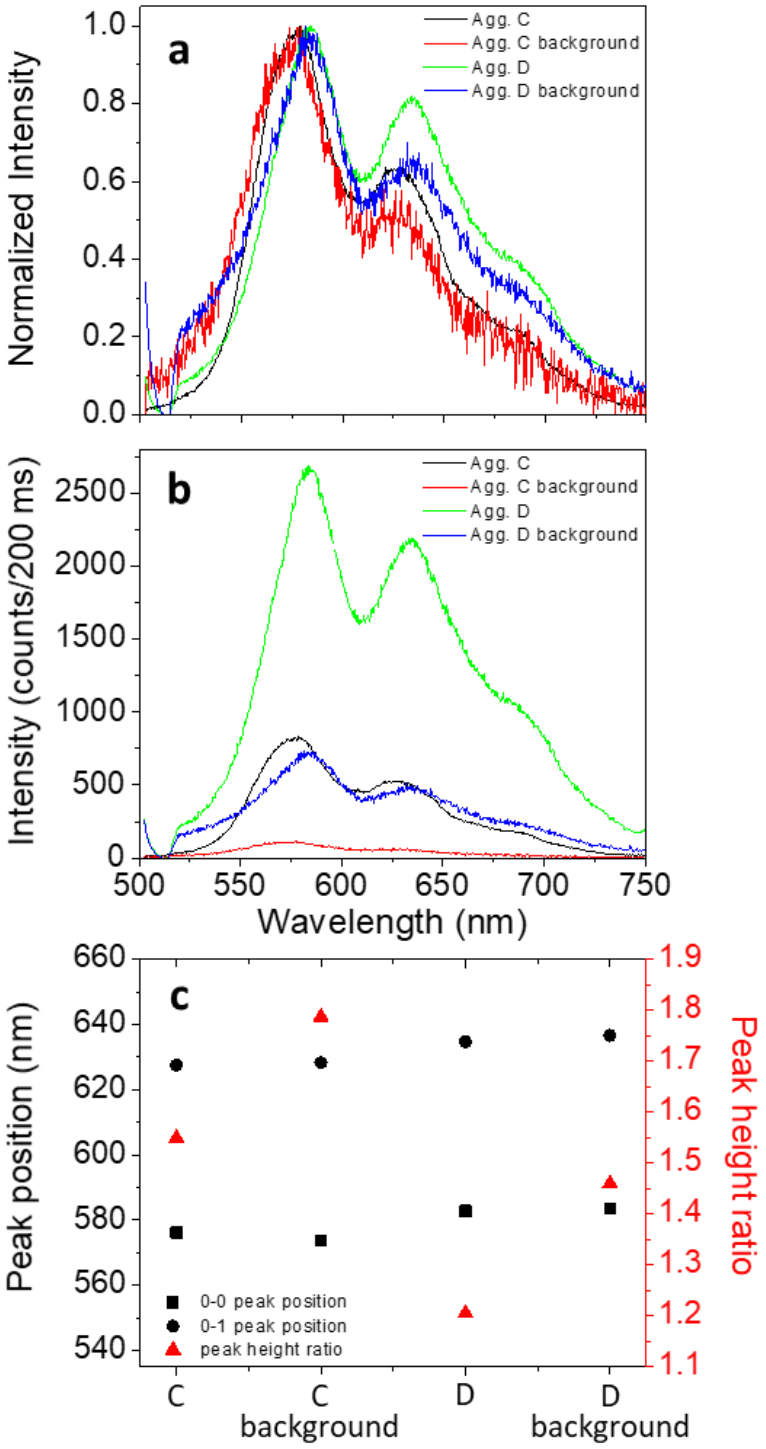

Figure 28. (a) Normalized average spectra of aggregates C and D together with spectra collected from the background between features following SVA. The excitation power densities were 330 W/cm^2 for aggregates C and their background and 88.7 W/cm^2 for aggregates D and their background. (b) The same spectra as (a) but without normalization. (c) (Black square) 0-0 and (black circle) 0-1 peak positions and (red triangle) 0-0/0-1 peak height ratios of aggregates C and D and their backgrounds obtained from spectra shown above.

aggregation suggests this spectral shift reflects local effects that do not extend across larger aggregates, in contrast to findings in toluene-prepared aggregates. This is also supported by the decrease of the 0-0/0-1 peak ratio as a function of increasing aggregate size, consistent with interchain coupling in the presence of disorder, as captured by the description of MEH-PPV aggregates as strongly disordered HJ-aggregates.[36,134] Similarly, increasing quenching efficiency as a function of aggregate size need not indicate efficient packing through intermolecular contacts that facilitate exciton transport, as such quenching, which reflects new nonradiative pathways available, may also be local in nature. This is consistent with an earlier finding showing that MEH-PPV aggregates coalescence, a process that diminishes order in the aggregates and is suggested to occur through a point and at random orientation, also leading to quenching.[80]

Finally, it is interesting to note that while the most notable spectral changes occur between single molecules and small aggregates A, spectral shift continues as a function of aggregate size, evolving even between aggregates C and D, with the spectrum of aggregate D quite similar to spectra of thin films of MEH-PPV, with reported 0-0 peak positions of ~585 nm.[56,147] The additional red shift, together with decrease in the 0-0/0-1 peak ratio, between aggregates C and D indicate a transition from individual aggregate to bulk film properties between aggregates of several hundred chains and those of over a thousand single chains for the preparation conditions used here, which include initial dissolution in a good solvent followed by swelling in a mix of solvents that supports a combination of Ostwald ripening, shown in some contexts to support chain ordering, and coalescence, shown to limit photophysical anisotropy and exciton diffusion.[76,80]

3.4 Conclusion

Our study showed self-assembly of largely isotropic aggregates of MEH-PPV via controlled and reproducible solvent vapor swelling of an inert polymer matrix seeded with

dispersed single MEH-PPV chains. Polarization modulation histograms indicate that aggregates templated on molecules initially showing low compaction and limited transition dipole alignment maintain those characteristics even when the single-molecule conformation is set only by choice of initial dissolving solvent. The poor compaction of the aggregate limits enhancement of exciton diffusion in these aggregates relative to single molecules, as reflected in fluorescence transients that do not show evidence of long length scale exciton diffusion. However, sufficient new intermolecular interactions emerge to red shift the spectrum of aggregates relative to single molecules, with aggregates comprised of just a few molecules already showing notable spectral changes relative to isolated molecules. Aggregates composed of few to more than a thousand single molecules show additional spectral evolution as a function of aggregate size, both red shifting and showing a decreased ratio of 0-0 to 0-1 peak intensities. Taken together these results suggest locally enhanced exciton diffusion upon aggregation of a few molecules but limited enhancement of that effect upon further aggregation, as ordering that occurs in few molecule aggregates does not extend over longer distances and larger structures.

Chapter 4. Conclusion and Outlook

Conjugated polymers are of interest for a growing array of commercial devices. The link between conformation and photophysical properties in conjugated polymers has been extensively studied for almost two decades; however, understanding of exciton behavior in environments relevant to devices is still lacking due to the existence of a large number of chromophores and conformational heterogeneity, resulting in complexity both intra- and inter-molecularly. In Chapter 2, an interesting and previously overlooked phenomenon in a commonly used experimental technique was described. We showed that the sublinearity of MEH-PPV single-molecule fluorescence intensity as a function of excitation intensity due to quenching can lead to misinterpretation of polarization modulation depth measurement data, which in turn can result in misjudgment of single-molecule conformation. In Chapter 3, the impact of solvent vapor annealing on single-molecule conformation and the photophysical properties of nearly isotropic aggregates of varying sizes were described. First, we showed that the initial single-molecule conformation determined by the dissolving solvent is largely maintained after solvent vapor swelling and deswelling, even with sufficient swelling to allow for conjugated polymer chain mobility. Next, we observed that nearly isotropic aggregates consisting of a few to several hundred conjugated polymer chains show locally enhanced exciton diffusion, manifested by red-shifted emission and the change in spectral peak ratio.

Several follow-up studies are suggested by the work presented here. Following Chapter 3, it would be interesting to explore whether single-molecule morphology is maintained even in the larger fibrillar structures and percolated networks that have been demonstrated previously[148] and resemble conjugated polymer pattern formation as it occurs in bulk heterojunction devices. Moreover, the general applicability and power of the single-molecule and single-particle studies

described in this dissertation suggest bringing these techniques and approaches to other multi-chromophoric systems of interest in materials chemistry.

References

1. Mikhnenko, O. V., Blom, P. W. M. & Nguyen, T.-Q. Exciton diffusion in organic semiconductors. *Energy Environ. Sci.* **8**, 1867–1888 (2015).
2. Abbaszadeh, D. *et al.* Electron trapping in conjugated polymers. *Chem. Mater.* **31**, 6380–6386 (2019).
3. Kuik, M. *et al.* Charge Transport and Recombination in Polymer Light-Emitting Diodes. *Adv. Mater.* **26**, 512–531 (2014).
4. Günes, S., Neugebauer, H. & Sariciftci, N. S. Conjugated Polymer-Based Organic Solar Cells. *Chem. Rev.* **107**, 1324–1338 (2007).
5. Coakley, K. M. & McGehee, M. D. Conjugated polymer photovoltaic cells. *Chem. Mater.* **16**, 4533–4542 (2004).
6. Liang, Y. & Yu, L. A New Class of Semiconducting Polymers for Bulk Heterojunction Solar Cells with Exceptionally High Performance. *Acc. Chem. Res.* **43**, 1227–1236 (2010).
7. Hou, W., Xiao, Y., Han, G. & Lin, J.-Y. The Applications of Polymers in Solar Cells: A Review. *Polymers (Basel).* **11**, 143 (2019).
8. Friend, R. H. *et al.* Electroluminescence in conjugated polymers. *Nature* **397**, 121–128 (1999).
9. Zheng, H. *et al.* All-solution processed polymer light-emitting diode displays. *Nat. Commun.* **4**, 1971 (2013).
10. Sekine, C., Tsubata, Y., Yamada, T., Kitano, M. & Doi, S. Recent progress of high performance polymer OLED and OPV materials for organic printed electronics. *Sci. Technol. Adv. Mater.* **15**, (2014).
11. Yang, J., Zhao, Z., Wang, S., Guo, Y. & Liu, Y. Insight into High-Performance Conjugated

Polymers for Organic Field-Effect Transistors. *Chem* **4**, 2748–2785 (2018).

12. Facchetti, A. π-Conjugated polymers for organic electronics and photovoltaic cell applications. *Chem. Mater.* **23**, 733–758 (2011).
13. Zhou, H., Yang, L. & You, W. Rational design of high performance conjugated polymers for organic solar cells. *Macromolecules* **45**, 607–632 (2012).
14. Benten, H., Mori, D., Ohkita, H. & Ito, S. Recent research progress of polymer donor/ polymer acceptor blend solar cells. *J. Mater. Chem. A* **1**, 5439–5776 (2013).
15. Rathgeber, S., De Toledo, D. B., Birckner, E., Hoppe, H. & Egbe, D. A. M. Intercorrelation between structural ordering and emission properties in photoconducting polymers. *Macromolecules* **43**, 306–315 (2010).
16. Dyson, M. J. *et al.* Managing Local Order in Conjugated Polymer Blends via Polarity Contrast. *Chem. Mater.* **31**, 6540–6547 (2019).
17. Kuei, B. & Gomez, E. D. Chain conformations and phase behavior of conjugated polymers. *Soft Matter* **13**, 49–67 (2017).
18. Adachi, T. *et al.* Regioregularity and single polythiophene chain conformation. *J. Phys. Chem. Lett.* **2**, 1400–1404 (2011).
19. Hu, Z. *et al.* Effect of the side-chain-distribution density on the single-conjugated-polymer-chain conformation. *ChemPhysChem* **14**, 4143–8 (2013).
20. Botiz, I., Astilean, S. & Stingelin, N. Altering the emission properties of conjugated polymers. *Polym. Int.* **65**, 157–163 (2016).
21. Hu, Z., Shao, B., Geberth, G. T. & Vanden Bout, D. A. Effects of Molecular Architecture on Morphology and Photophysics in Conjugated Polymers: from Single Molecules to Bulk. *Chem. Sci.* **9**, 1101–1111 (2018).

22. Dimitrov, S. D. *et al.* Singlet exciton lifetimes in conjugated polymer films for organic solar cells. *Polymers (Basel).* **8**, 14 (2016).

23. Scholes, G. D. & Rumbles, G. Excitons in nanoscale systems. *Nat. Mater.* **5**, 683–696 (2006).

24. Köhler, A. & Bässler, H. *Electronic processes in organic semiconductors: An introduction*. (Wiley-VCH, 2015). doi:10.1002/9783527685172

25. Deng, X.-Y. Light-Emitting Devices with Conjugated Polymers. *Int. J. Mol. Sci.* **12**, 1575–1594 (2011).

26. Hu, D. *et al.* Collapse of stiff conjugated polymers with chemical defects into ordered, cylindrical conformations. *Nature* **405**, 1030–3 (2000).

27. Lupton, J. M. Chromophores in conjugated polymers - All straight? *ChemPhysChem* **13**, 901–907 (2012).

28. Schwartz, B. J. Conjugated polymers: what makes a chromophore? *Nat. Mater.* **7**, 427–428 (2008).

29. Wong, K. F. *et al.* Structural and electronic characterization of chemical and conformational defects in conjugated polymers. *J. Phys. Chem. B* **105**, 6103–6107 (2001).

30. Hennebicq, E., De Leener, C., Brédas, J.-L., Scholes, G. D. & Beljonne, D. Chromophores in phenylenevinylene-based conjugated polymers: Role of conformational kinks and chemical defects. *J. Chem. Phys.* **125**, (2006).

31. Dykstra, T. E. *et al.* Conformational disorder and ultrafast exciton relaxation in PPV-family conjugated polymers. *J. Phys. Chem. B* **113**, 656–667 (2009).

32. Schwartz, B. J. CONJUGATED POLYMERS AS MOLECULAR MATERIALS: How Chain Conformation and Film Morphology Influence Energy Transfer and Interchain

Interactions. *Annu. Rev. Phys. Chem.* **54**, 141–172 (2003).

33. Bounos, G. *et al.* Controlling chain conformation in conjugated polymers using defect inclusion strategies. *J. Am. Chem. Soc.* **133**, 10155–10160 (2011).

34. Dubay, K. H. *et al.* Accurate force field development for modeling conjugated polymers. *J. Chem. Theory Comput.* **8**, 4556–4569 (2012).

35. Schindler, F. *et al.* Counting chromophores in conjugated polymers. *Angew. Chemie Int. Ed.* **44**, 1520–1525 (2005).

36. Köhler, A., Hoffmann, S. T. & Bässler, H. An order-disorder transition in the conjugated polymer MEH-PPV. *J. Am. Chem. Soc.* **134**, 11594–11601 (2012).

37. Khoshkhoo, M. S., Taromi, F. A., Kowsari, E. & Shalamzari, E. K. Contribution of chromophores with different numbers of repeat units to overall emission of MEH-PPV: An experimental and simulation study. *Polymer (Guildf).* **54**, 4017–4029 (2013).

38. Panzer, F., Bässler, H. & Köhler, A. Temperature Induced Order-Disorder Transition in Solutions of Conjugated Polymers Probed by Optical Spectroscopy. *J. Phys. Chem. Lett.* **8**, 114–125 (2017).

39. Mark, J. E. *Physical Properties of Polymers Handbook*. (Springer, 2006).

40. Lupton, J. M. Single-molecule spectroscopy for plastic electronics: Materials analysis from the bottom-up. *Adv. Mater.* **22**, 1689–1721 (2010).

41. Barbara, P. F., Gesquiere, A. J., Park, S.-J. & Lee, Y. J. Single-molecule spectroscopy of conjugated polymers. *Acc. Chem. Res.* **38**, 602–610 (2005).

42. Scholes, G. D., Larsen, D. S., Fleming, G. R. & Rumbles, G. Origin of line broadening in the electronic absorption spectra of conjugated polymers: Three-pulse-echo studies of MEH-PPV in toluene. *Phys. Rev. B - Condens. Matter Mater. Phys.* **61**, 13670–13678

(2000).

43. Hwang, I. & Scholes, G. D. Electronic energy transfer and quantum-coherence in π-conjugated polymers. *Chem. Mater.* **23**, 610–620 (2011).

44. Bässler, H. & Schweitzer, B. Site-selective fluorescence spectroscopy of conjugated polymers and oligomers. *Acc. Chem. Res.* **32**, 173–182 (1999).

45. Janse van Rensburg, E. J., Guillet, J. E. & Whittington, S. G. Exciton Migration on Polymers. *Macromolecules* **22**, 4212–4220 (1989).

46. Holmes, R. J. Enhancing energy transport in conjugated polymers. *Science (80-.).* **360**, 854–855 (2018).

47. Scheblykin, I. G., Yartsev, A., Pullerits, T., Gulbinas, V. & Sundström, V. Excited state and charge photogeneration dynamics in conjugated polymers. *J. Phys. Chem. B* **111**, 6303–6321 (2007).

48. Yu, J., Hu, D. & Barbara, P. F. Unmasking electronic energy transfer of conjugated polymers by suppression of O2 quenching. *Science (80-.).* **289**, 1327–1330 (2000).

49. Scholz, S., Kondakov, D., Lüssem, B. & Leo, K. Degradation mechanisms and reactions in organic light-emitting devices. *Chem. Rev.* **115**, 8449–8503 (2015).

50. Park, S.-J., Gesquiere, A. J., Yu, J. & Barbara, P. F. Charge Injection and Photooxidation of Single Conjugated Polymer Molecules. *J. Am. Chem. Soc.* **126**, 4116–4117 (2004).

51. Scurlock, R. D., Wang, B., Ogilby, P. R., Sheats, J. R. & Clough, R. L. Singlet Oxygen as a Reactive Intermediate in the Photodegradation of an Electroluminescent Polymer. *J. Am. Chem. Soc.* **117**, 10194–10202 (1995).

52. De Jong, M. J. M. & Vissenberg, M. C. J. M. Theory of luminescence quenching and photobleaching in conjugated polymers. *Philips J. Res.* **51**, 495–510 (1998).

53. Vanden Bout, D. A. *et al.* Discrete Intensity Jumps and Intramolecular Electronic Energy Transfer in the Spectroscopy of Single Conjugated Polymer Molecules. *Science (80-.).* **277**, 1074–1077 (1997).

54. Yu, J., Lammi, R., Gesquiere, A. J. & Barbara, P. F. Singlet−triplet and triplet−triplet interactions in conjugated polymer single molecules. *J. Phys. Chem. B* **109**, 10025–34 (2005).

55. Steiner, F., Vogelsang, J. & Lupton, J. M. Singlet-triplet annihilation limits exciton yield in poly(3-hexylthiophene). *Phys. Rev. Lett.* **112**, 1–5 (2014).

56. Nguyen, T.-Q., Martini, I. B., Liu, J. & Schwartz, B. J. Controlling Interchain Interactions in Conjugated Polymers: The Effects of Chain Morphology on Exciton−Exciton Annihilation and Aggregation in MEH−PPV Films. *J. Phys. Chem. B* **104**, 237–255 (2000).

57. Wöll, D. *et al.* Polymers and single molecule fluorescence spectroscopy, what can we learn? *Chem. Soc. Rev.* **38**, 313–328 (2009).

58. Kulzer, F. & Orrit, M. Single-Molecule Optics. *Annu. Rev. Phys. Chem.* **55**, 585–611 (2004).

59. Kobayashi, H., Onda, S., Furumaki, S., Habuchi, S. & Vacha, M. A single-molecule approach to conformation and photophysics of conjugated polymers. *Chem. Phys. Lett.* **528**, 1–6 (2012).

60. Feist, F. A., Tommaseo, G. & Basché, T. Single-molecule spectroscopy of MEH-PPV polymer molecules in different host matrices. *J. Phys. Chem. C* **113**, 11484–11490 (2009).

61. Huang, B., Bates, M. & Zhuang, X. Super-Resolution Fluorescence Microscopy. *Annu. Rev. Biochem.* **78**, 993–1016 (2009).

62. Shen, H. *et al.* Single Particle Tracking: From Theory to Biophysical Applications. *Chem.*

Rev. **117**, 7331–7376 (2017).

63. von Diezmann, A., Shechtman, Y. & Moerner, W. E. Three-Dimensional Localization of Single Molecules for Super-Resolution Imaging and Single-Particle Tracking. *Chem. Rev.* **117**, 7244–7275 (2017).

64. Vogelsang, J., Brazard, J., Adachi, T., Bolinger, J. C. & Barbara, P. F. Watching the Annealing Process One Polymer Chain at a Time. *Angew. Chemie Int. Ed.* **50**, 2257–2261 (2011).

65. Huser, T., Yan, M. & Rothberg, L. J. Single chain spectroscopy of conformational dependence of conjugated polymer photophysics. *Proc. Natl. Acad. Sci. U. S. A.* **97**, 11187–11191 (2000).

66. Grey, J. K. *et al.* Effect of temperature and chain length on the bimodal emission properties of single polyfluorene copolymer molecules. *J. Phys. Chem. B* **110**, 18898–18903 (2006).

67. Yu, Z. & Barbara, P. F. Low-temperature single-molecule spectroscopy of MEH-PPV conjugated polymer molecules. *J. Phys. Chem. B* **108**, 11321–11326 (2004).

68. Traub, M. C., Lakhwani, G., Bolinger, J. C., Vanden Bout, D. A. & Barbara, P. F. Electronic energy transfer in highly aligned MEH-PPV single chains. *J. Phys. Chem. B* **115**, 9941–9947 (2011).

69. Mirzov, O. *et al.* Polarization portraits of single multichromophoric systems: Visualizing conformation and energy transfer. *Small* **5**, 1877–1888 (2009).

70. Mehta, A. *et al.* Oriented nanostructures from single molecules of a semiconducting polymer: Polarization evidence for highly aligned intramolecular geometries. *Nano Lett.* **3**, 603–607 (2003).

71. Wöll, D. & Flors, C. Super-resolution Fluorescence Imaging for Materials Science. *Small*

Methods **1**, 1700191 (2017).

72. Habuchi, S., Onda, S. & Vacha, M. Mapping the emitting sites within a single conjugated polymer molecule. *Chem. Commun.* **32**, 4868–70 (2009).

73. Habuchi, S., Onda, S. & Vacha, M. Molecular weight dependence of emission intensity and emitting sites distribution within single conjugated polymer molecules. *Phys. Chem. Chem. Phys.* **13**, 1743–53 (2011).

74. Vacha, M. & Habuchi, S. Conformation and physics of polymer chains: a single-molecule perspective. *NPG Asia Mater.* **2**, 134–142 (2010).

75. Park, H., Hoang, D. T., Paeng, K. & Kaufman, L. J. Localizing Exciton Recombination Sites in Conformationally Distinct Single Conjugated Polymers by Super-resolution Fluorescence Imaging. *ACS Nano* **9**, 3151–3158 (2015).

76. Vogelsang, J., Adachi, T., Brazard, J., Vanden Bout, D. A. & Barbara, P. F. Self-assembly of highly ordered conjugated polymer aggregates with long-range energy transfer. *Nat. Mater.* **10**, 942–6 (2011).

77. Hu, Z. *et al.* Excitonic energy migration in conjugated polymers: The critical role of interchain morphology. *J. Am. Chem. Soc.* **136**, 16023–16031 (2014).

78. Hu, Z. *et al.* Impact of backbone fluorination on nanoscale morphology and excitonic coupling in polythiophenes. *Proc. Natl. Acad. Sci. U. S. A.* **114**, 5113–5118 (2017).

79. Yang, J., Park, H. & Kaufman, L. J. Highly Anisotropic Conjugated Polymer Aggregates: Preparation and Quantification of Physical and Optical Anisotropy. *J. Phys. Chem. C* **121**, 13854–13862 (2017).

80. Yang, J., Park, H. & Kaufman, L. J. In Situ Optical Imaging of the Growth of Conjugated Polymer Aggregates. *Angew. Chemie Int. Ed.* **75429**, 1826–1830 (2018).

81. Grey, J. K., Kim, D. Y., Norris, B. C., Miller, W. L. & Barbara, P. F. Size-dependent spectroscopic properties of conjugated polymer nanoparticles. *J. Phys. Chem. B* **110**, 25568–25572 (2006).

82. Lin, H. *et al.* Single chain versus single aggregate spectroscopy of conjugated polymers. Where is the border? *Phys. Chem. Chem. Phys.* **12**, 11770–7 (2010).

83. Vogelsang, J. & Lupton, J. M. Solvent Vapor Annealing of Single Conjugated Polymer Chains: Building Organic Optoelectronic Materials from the Bottom Up. *J. Phys. Chem. Lett.* **3**, 1503–1513 (2012).

84. Traub, M. C. *et al.* Unmasking bulk exciton traps and interchain electronic interactions with single conjugated polymer aggregates. *ACS Nano* **6**, 523–529 (2012).

85. Stangl, T. *et al.* Mesoscopic quantum emitters from deterministic aggregates of conjugated polymers. *Proc. Natl. Acad. Sci. U. S. A.* **112**, E5560–E5566 (2015).

86. Eder, T. *et al.* Switching between H- and J-type electronic coupling in single conjugated polymer aggregates. *Nat. Commun.* **8**, 1641 (2017).

87. Steiner, F., Lupton, J. M. & Vogelsang, J. Role of Triplet-State Shelving in Organic Photovoltaics: Single-Chain Aggregates of Poly(3-hexylthiophene) versus Mesoscopic Multichain Aggregates. *J. Am. Chem. Soc.* **139**, 9787–9790 (2017).

88. Sinturel, C., Vayer, M., Morris, M. A. & Hillmyer, M. A. Solvent Vapor Annealing of Block Polymer Thin Films. *Macromolecules* **46**, 5399–5415 (2013).

89. Gotrik, K. W. *et al.* Morphology Control in Block Copolymer Films Using Mixed Solvent Vapors. *ACS Nano* **6**, 8052–8059 (2012).

90. Albert, J. N. L. & Epps, T. H. Self-assembly of block copolymer thin films. *Mater. Today* **13**, 24–33 (2010).

91. Jin, C., Olsen, B. C., Luber, E. J. & Buriak, J. M. Nanopatterning via solvent vapor annealing of block copolymer thin films. *Chem. Mater.* **29**, 176–188 (2017).

92. Hoang, D. T. *et al.* In situ multi-modal monitoring of solvent vapor swelling in polymer thin films. *Rev. Sci. Instrum.* **87**, 015106 (2016).

93. Park, H., Kwon, Y. & Kaufman, L. J. Complex Photophysical Behaviors Affect Single Conjugated Molecule Optical Anisotropy Measurements. *J. Phys. Chem. C* **123**, 1960–1965 (2019).

94. Ha, T., Enderle, T., Chemla, D. S., Selvin, P. R. & Weiss, S. Single molecule dynamics studied by polarization modulation. *Phys. Rev. Lett.* **77**, 3979–3982 (1996).

95. Ha, T., Laurence, T. A., Chemla, D. S. & Weiss, S. Polarization Spectroscopy of Single Fluorescent Molecules. *J. Phys. Chem. B* **103**, 6839–6850 (1999).

96. Harms, G. S., Sonnleitner, M., Schütz, G. J., Gruber, H. J. & Schmidt, T. Single-molecule anisotropy imaging. *Biophys. J.* **77**, 2864–2870 (1999).

97. Gradinaru, C. C., Marushchak, D. O., Samim, M. & Krull, U. J. Fluorescence anisotropy: From single molecules to live cells. *Analyst* **135**, 452–459 (2010).

98. Ebihara, Y. & Vacha, M. Relating conformation and photophysics in single MEH-PPV chains. *J. Phys. Chem. B* **112**, 12575–12578 (2008).

99. Furumaki, S., Habuchi, S. & Vacha, M. Fluorescence-detected three-dimensional linear dichroism: A method to determine absorption anisotropy in single sub-wavelength size nanoparticles. *Chem. Phys. Lett.* **487**, 312–314 (2010).

100. Furumaki, S. *et al.* Absorption linear dichroism measured directly on a single light-harvesting system: The role of disorder in chlorosomes of green photosynthetic bacteria. *J. Am. Chem. Soc.* **133**, 6703–6710 (2011).

101. Warshaw, D. M. *et al.* Myosin conformational states determined by single fluorophore polarization. *Proc. Natl. Acad. Sci. U. S. A.* **95**, 8034–8039 (1998).

102. Ying, L. & Xie, X. S. Fluorescence Spectroscopy, Exciton Dynamics, and Photochemistry of Single Allophycocyanin Trimers. *J. Phys. Chem. B* **102**, 10399–10409 (1998).

103. Thiessen, A. *et al.* Unraveling the chromophoric disorder of poly(3-hexylthiophene). *Proc. Natl. Acad. Sci. U. S. A.* **110**, E3550-6 (2013).

104. Chen, P. Y., Rassamesard, A., Chen, H. L. & Chen, S.-A. Conformation and fluorescence property of poly(3-hexylthiophene) isolated chains studied by single molecule spectroscopy: Effects of solvent quality and regioregularity. *Macromolecules* **46**, 5657–5663 (2013).

105. Traub, M. C. *et al.* Chromophore-controlled self-assembly of highly ordered polymer nanostructures. *J. Phys. Chem. Lett.* **4**, 2520–2524 (2013).

106. Park, H., Hoang, D. T., Paeng, K., Yang, J. & Kaufman, L. J. Conformation-Dependent Photostability among and within Single Conjugated Polymers. *Nano Lett.* **15**, 7604–7609 (2015).

107. Thomsson, D., Lin, H. & Scheblykin, I. G. Correlation analysis of fluorescence intensity and fluorescence anisotropy fluctuations in single-molecule spectroscopy of conjugated polymers. *ChemPhysChem* **11**, 897–904 (2010).

108. Adachi, T. *et al.* Conformational effect on energy transfer in single polythiophene chains. *J. Phys. Chem. B* **116**, 9866–9872 (2012).

109. Camacho, R., Thomsson, D., Sforazzini, G., Anderson, H. L. & Scheblykin, I. G. Inhomogeneous quenching as a limit of the correlation between fluorescence polarization and conformation of single molecules. *J. Phys. Chem. Lett.* **4**, 1053–1058 (2013).

110. Hale, G. D., Oldenburg, S. J. & Halas, N. J. Observation of triplet exciton dynamics in conjugated polymer films using two-photon photoelectron spectroscopy. *Phys. Rev. B* **55**, R16069–R16071 (1997).

111. Hou, L., Adhikari, S., Tian, Y., Scheblykin, I. G. & Orrit, M. Absorption and Quantum Yield of Single Conjugated Polymer Poly[2-methoxy-5-(2-ethylhexyloxy)-1,4-phenylenevinylene] (MEH-PPV) Molecules. *Nano Lett.* **17**, 1575–1581 (2017).

112. Hader, K., Consani, C., Brixner, T. & Engel, V. Mapping of exciton–exciton annihilation in MEH-PPV by time-resolved spectroscopy: experiment and microscopic theory. *Phys. Chem. Chem. Phys.* **19**, 31989–31996 (2017).

113. Sahoo, D., Tian, Y., Sforazzini, G., Anderson, H. L. & Scheblykin, I. G. Photo-induced fluorescence quenching in conjugated polymers dispersed in solid matrices at low concentration. *J. Mater. Chem. C* **2**, 6601–6608 (2014).

114. Hooley, E. N., Tilley, A. J., White, J. M., Ghiggino, K. P. & Bell, T. D. M. Energy transfer in PPV-based conjugated polymers: a defocused widefield fluorescence microscopy study. *Phys. Chem. Chem. Phys.* **16**, 7108–7114 (2014).

115. Martini, I. B., Smith, A. D. & Schwartz, B. J. Exciton-exciton annihilation and the production of interchain species in conjugated polymer films: Comparing the ultrafast stimulated emission and photoluminescence dynamics of MEH-PPV. *Phys. Rev. B* **69**, 035204 (2004).

116. Barzykin, A. V. & Tachiya, M. Stochastic model of photodynamics in multichromophoric conjugated polymers. *J. Phys. Chem. B* **110**, 7068–7072 (2006).

117. Juzeliūnas, G. Time-dependent fluorescence depolarization arising from exciton annihilation in confined molecular domains. *Chem. Phys.* **151**, 169–178 (1991).

118. Scheblykin, I. G. *et al.* Non-coherent exciton migration in J-aggregates of the dye THIATS: Exciton-exciton annihilation and fluorescence depolarization. *Chem. Phys. Lett.* **298**, 341–350 (1998).

119. Crocker, J. C. & Grier, D. G. Methods of Digital Video Microscopy for Colloidal Studies. *J. Colloid Interface Sci.* **179**, 298–310 (1996).

120. Kwon, Y. & Kaufman, L. J. Nearly Isotropic Conjugated Polymer Aggregates with Efficient Local Exciton Diffusion. *J. Phys. Chem. C* **123**, 29418–29426 (2019).

121. Kaake, L. G., Barbara, P. F. & Zhu, X. Intrinsic charge trapping in organic and polymeric semiconductors: A physical chemistry perspective. *J. Phys. Chem. Lett.* **1**, 628–635 (2010).

122. Lu, L. & Yu, L. Understanding low bandgap polymer PTB7 and optimizing polymer solar cells based on it. *Adv. Mater.* **26**, 4413–4430 (2014).

123. Bardeen, C. J. Exciton Quenching and Migration in Single Conjugated Polymers. *Science (80-.).* **331**, 544–545 (2011).

124. Rothberg, L. J. *et al.* Photophysics of phenylenevinylene polymers. *Synth. Met.* **80**, 41–58 (1996).

125. Adachi, T., Vogelsang, J. & Lupton, J. M. Unraveling the electronic heterogeneity of charge traps in conjugated polymers by single-molecule spectroscopy. *J. Phys. Chem. Lett.* **5**, 573–577 (2014).

126. Lee, H., Park, C., Sin, D. H., Park, J. H. & Cho, K. Recent advances in morphology optimization for organic photovoltaics. *Adv. Mater.* **30**, 1–39 (2018).

127. Jung, E. H. *et al.* Efficient, stable and scalable perovskite solar cells using poly(3-hexylthiophene). *Nature* **567**, 511–515 (2019).

128. Becker, K. *et al.* How chromophore shape determines the spectroscopy of phenylene-

vinylenes: Origin of spectral broadening in the absence of aggregation. *J. Phys. Chem. B* **112**, 4859–4864 (2008).

129. Schindler, F. & Lupton, J. M. Single chromophore spectroscopy of MEH-PPV: Homing-in on the elementary emissive species in conjugated polymers. *ChemPhysChem* **6**, 926–934 (2005).

130. Adachi, T. *et al.* Highly Ordered Single Conjugated Polymer Chain Rod Morphologies. *J. Phys. Chem. C* **114**, 20896–20902 (2010).

131. Hu, D., Yu, J. & Barbara, P. F. Single-molecule spectroscopy of the conjugated polymer MEH-PPV. *J. Am. Chem. Soc.* **121**, 6936–6937 (1999).

132. Hollars, C. W., Lane, S. M. & Huser, T. Controlled non-classical photon emission from single conjugated polymer molecules. *Chem. Phys. Lett.* **370**, 393–398 (2003).

133. Feist, F. A., Tommaseo, G. & Basché, T. Observation of very narrow linewidths in the fluorescence excitation spectra of single conjugated polymer chains at 1.2 K. *Phys. Rev. Lett.* **98**, 1–4 (2007).

134. Yamagata, H. *et al.* The red-phase of poly[2-methoxy-5-(2-ethylhexyloxy)-1,4-phenylenevinylene] (MEH-PPV): A disordered HJ-aggregate. *J. Chem. Phys.* **139**, 114903 (2013).

135. Traiphol, R., Sanguansat, P., Srikhirin, T., Kerdcharoen, T. & Osotchan, T. Spectroscopic study of photophysical change in collapsed coils of conjugated polymers: Effects of solvent and temperature. *Macromolecules* **39**, 1165–1172 (2006).

136. Liang, J. J. *et al.* Heterogeneous energy landscapes of individual luminescent conjugated polymers. *Phys. Rev. B* **74**, 1–9 (2006).

137. Ferdous, S. *et al.* New Insights into Morphology of High Performance BHJ Photovoltaics

Revealed by High Resolution AFM. *Nano Lett.* **14**, 5727–5732 (2014).

138. Spano, F. C. & Silva, C. H- and J-aggregate behavior in polymeric semiconductors. *Annu. Rev. Phys. Chem.* **65**, 477–500 (2014).

139. Tenopala-carmona, F., Fronk, S., Bazan, G. C., Samuel, I. D. W. & Penedo, J. C. Real-time observation of conformational switching in single conjugated polymer chains. *Sci. Adv.* **4**, eaao5786 (2018).

140. Tian, Y., Sheinin, V., Kulikova, O., Mamardashvili, N. & Scheblykin, I. G. Improving photo-stability of conjugated polymer MEH-PPV embedded in solid matrices by purification of the matrix polymer. *Chem. Phys. Lett.* **599**, 142–145 (2014).

141. Neef, C. J. & Ferraris, J. P. MEH-PPV: Improved synthetic procedure and molecular weight control. *Macromolecules* **33**, 2311–2314 (2000).

142. Ebihara, Y., Habuchi, S. & Vacha, M. Conformation-dependent Room-temperature Emission Spectra of Single MEH-PPV Chains in Different Polymer Matrices. *Chem. Lett.* **38**, 1094–1095 (2009).

143. Kim, D. Y., Grey, J. K. & Barbara, P. F. A detailed single molecule spectroscopy study of the vibronic states and energy transfer pathways of the conjugated polymer MEH-PPV. *Synth. Met.* **156**, 336–345 (2006).

144. Feist, F. A., Zickler, M. F. & Basché, T. Origin of the red sites and energy transfer rates in single meh-ppv chains at low temperature. *ChemPhysChem* **12**, 1499–1508 (2011).

145. Collini, E. & Scholes, G. D. Electronic and vibrational coherences in resonance energy transfer along MEH-PPV chains at room temperature. *J. Phys. Chem. A* **113**, 4223–4241 (2009).

146. Ghosh, A. *et al.* Exciton Dynamics and Formation Mechanism of MEH-PPV Polymer-

Based Nanostructures. *J. Phys. Chem. C* **121**, 21062–21072 (2017).

147. Gaab, K. M. & Bardeen, C. J. Wavelength and Temperature Dependence of the Femtosecond Pump−Probe Anisotropies in the Conjugated Polymer MEH-PPV: Implications for Energy-Transfer Dynamics. *J. Phys. Chem. B* **108**, 4619–4626 (2004).

148. Haedler, A. T. *et al.* Long-range energy transport in single supramolecular nanofibres at room temperature. *Nature* **523**, 196–199 (2015).

149. Wirtz, D. Particle-Tracking Microrheology of Living Cells: Principles and Applications. *Annu. Rev. Biophys.* **38**, 301–326 (2009).

150. Sauerbrey, G. Verwendung von Schwingquarzen zur Wagungdiinner Schichten und zur Mikrowagung. *Zeitschrift fur Phys.* **155**, 206–222 (1959).

151. Kanazawa, K. K. & Gordonll, J. G. Frequency of a Quartz Microbalance in Contact with Liquid. *Anal. Chem.* **57**, 1770–1771 (1989).

152. Jung, Y. S. & Ross, C. A. Solvent-vapor-induced tunability of self-assembled block copolymer patterns. *Adv. Mater.* **21**, 2540–2545 (2009).

Appendix A. Experimental Details of Solvent Vapor Annealing

This chapter was reproduced in part from D. T. Hoang, J. Yang, K. Paeng, Y. Kwon, O. S. Kweon, and L. J. Kaufman, Rev. Sci. Instrum. ***87****, 015106 (2016) (Reference 92)*

A.1 Introduction

In this Appendix, we describe an apparatus for controlled delivery of solvent vapor to polymer thin film samples and simultaneous monitoring of multiple properties of those samples throughout the process of solvent vapor annealing. To achieve this multi-modal monitoring, two polymer thin films are prepared in an identical fashion and assessed in parallel adjacent to each other within a single sample chamber. One sample, prepared on a quartz crystal microbalance (QCM), is used to characterize the extent of swelling while another, prepared on a coverslip, is used for epifluorescence imaging. Swelling is performed in a controlled fashion using a series of mass-flow controllers (MFCs) to generate and control solvent vapor pressures. This approach to studying polymer films in their vapor swollen state allows simultaneous characterization of film swelling, viscoelasticity, structure, and/or dynamics under well-controlled conditions.

A.2 Apparatus

A.2.1 Solvent Vapor Annealing Chamber

The sample chamber is composed of three parts—the base, the body, and the lid—machined from aluminum. Within the sample chamber, two polymer thin films were prepared and assessed in parallel, with a coverslip-mounted sample at the chamber base and a QCM-mounted sample at the chamber lid (Figure 29). The base has an opening to hold a 25 mm diameter coverslip, sealed with Kalrez O-rings. The sample chamber lid is designed such that it can be fastened between the QCM crystal holder head and the retainer cover that holds the QCM in place (Figure 29c). The QCM sensor lies above and concentric to the imaged sample. An inlet and outlet for

vapor flow were bored through the sides of the cylinder body to allow connection to a MFC-regulated vapor flow system. The inlet and outlet to the sample chamber are controlled by two pin valves. The three components of the sample chamber are held together with bored-through screws with intercalating Kalrez O-rings to assure a good seal. In the experiments performed here, Teflon tape was applied around all junctures to further protect against possible leaks.

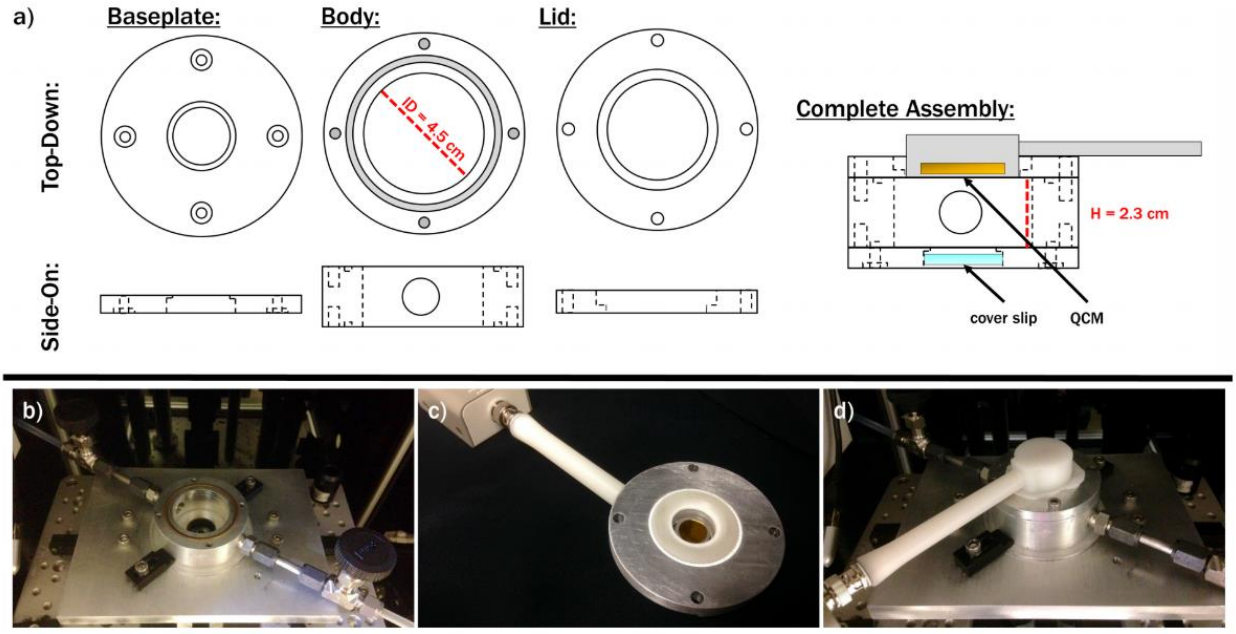

Figure 29. Schematic diagram of the chamber components both unassembled and assembled. (b–d) Photographs of the (b) sample chamber without lid, showing the coverslip in place over the objective lens, (c) underside of the chamber lid with the QCM attached, and (d) fully assembled chamber on the microscope sample stage.

A.2.2 Solvent Vapor Production

Solvent vapor was generated using a series of mass-flow controllers (Alicat Scientific MCS-100) to bubble dry nitrogen carrier gas through solvent reservoirs. In the configuration shown in Figure 30, two MFCs (MFC-A and MFC-B) control flow in two channels, though this system can be extended to more channels to support delivery of complex mixtures of solvents. A switch is present in each channel (S-A and S-B in Figure 30) to allow bypassing of the solvent reservoir connected to that channel. The flow of each channel is combined in a mixing bottle to

assure a reservoir of equilibrated vapor mixtures. Downstream from the mixing bottle, another switch (S-C) allows flow to or bypass of the sample chamber. Perfluoroalkoxy tubing (McMaster Carr; Ultraclear PFA Tubing, 1/8 in. inner diameter) was used to connect all the components involved with solvent vapor production and delivery since it is extremely resistant to a wide range of organic solvents.

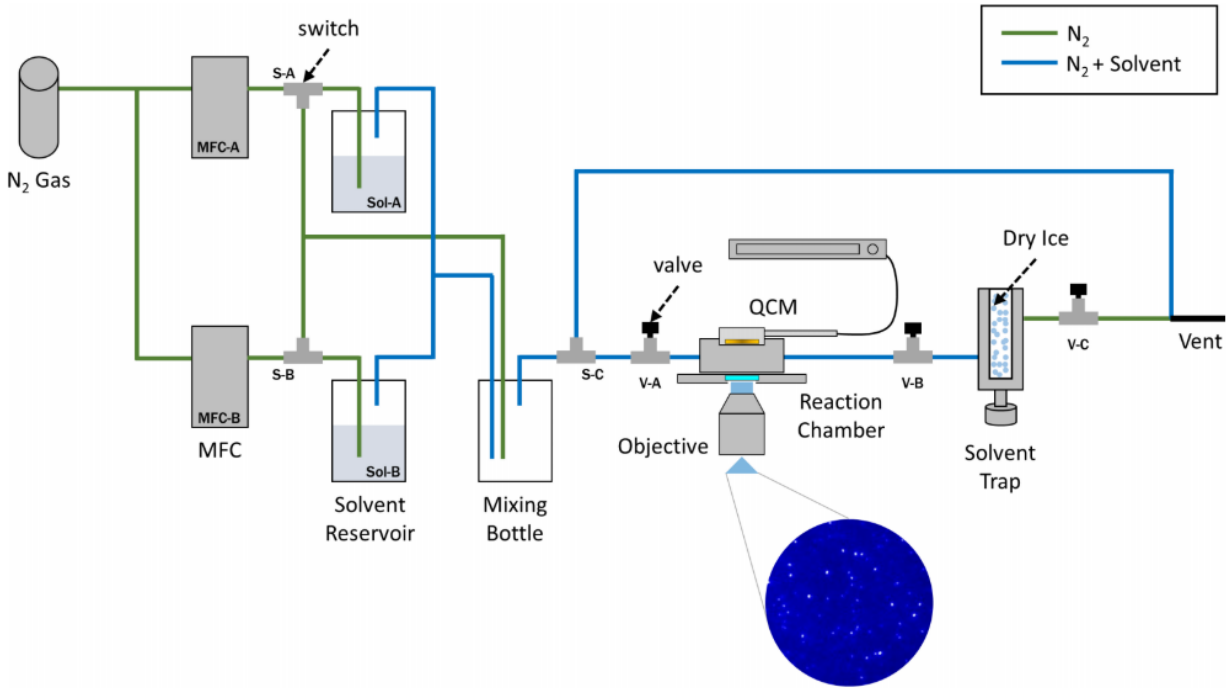

Figure 30. Schematic diagram of the solvent vapor delivery system. MFCs control the flow of carrier gas through the appropriate solvent reservoirs and the sample chamber. Switches and valves are present throughout (indicated by S- and V-, respectively) to direct and control flow. The vent at right is left open except in cases where the solvent trap is used to condense solvent vapors to assess quantity of solvent that was delivered to the sample.

A.2.3 Sample Characterization

The sample at the bottom of the chamber was prepared on a coverslip and was interrogated via wide-field epifluorescence microscopy, as it was described in Chapter 3.

In theory, the film employed for imaging could also be used to monitor film swelling through an optically based technique such as ellipsometry or interferometry. However, doing so could complicate fluorescence imaging; moreover, the film to be imaged must be prepared on a

coverslip, which is not ideal for these approaches. Instead, film thickness and swelling were assessed via parallel measurements on a film prepared on the QCM (Stanford Research Systems QCM-200) at the sample chamber's top. This measurement does not interfere with imaging, and the QCM is compact and simple to operate. Moreover, the QCM can return information on film viscoelasticity that can be used to validate storage and loss moduli obtained, for example, via particle tracking microrheology on the coverslip-mounted film.[149] Film thickness before and during SVA was assessed by measuring the decrease in resonance frequency from a bare QCM to one with a spin-cast film prior to or during swelling. The change in QCM resonance frequency reports film uptake of solvent via the Sauerbrey equation,

$$\Delta f = C_f \Delta m \qquad \text{Eq 9}$$

where Δf is the observed frequency change, C_f is the sensitivity factor for the crystal used, and Δm is the change of mass per area.[150] Change in mass per area can be transformed to film thickness (or change thereof) via

$$\Delta m = \rho \Delta h \qquad \text{Eq 10}$$

with ρ the density of the solvent responsible for the change in mass. To assure the (potentially evolving) viscoelasticity of the film does not affect measurement accuracy,[151] the QCM should be operated in a mode that corrects for resonance frequency changes due to viscoelastic losses.

A.3 Control of Vapor Pressure

A.3.1 Single Solvent Delivery

As depicted in Figure 30, solvent vapor was generated using MFCs to bubble dry nitrogen gas through solvent reservoirs. To assess the system's performance, expected and actual amounts of generated acetone vapor were compared.[89] The flow controllers allow direct control of *Q*, the

volumetric flow rate. The following equation describes the relationship between volumetric and molar flow rate:

$$M = Q\rho/M_w \qquad \text{Eq 11}$$

M is the molar flow rate, Q is the volumetric flow rate, ρ is the gas density, and M_w is the molecular weight of the gas. For nitrogen gas, employing Q_{nit} = 100 standard cm^3/min (sccm) yields M_{nit} = 4.147 × 10^{-3} mol/min. At this flow condition, the Reynolds number in the tubing used is 177, indicating laminar flow.

To calculate the molar flow rate for the solvent vapor, several assumptions were made. First, it was assumed that bubbling nitrogen gas through a solvent promotes solvent evaporation, ensuring that solvent vapor pressure remains at saturation (p_{sol}) for a given temperature. Because the solubility of nitrogen in common solvents is negligible, it was also assumed that M_{nit} remains constant after bubbling. Finally, the total pressure in the system was assumed to be 760 Torr because the SVA is an open system with low flow rates. Given these assumptions, the molar flow rate for solvent vapor (M_{sol}) for a MFC-controlled channel is given by

$$M_{sol} = M_{nit}\left[\frac{p_{sol}}{760 - p_{sol}}\right] \qquad \text{Eq 12}$$

Since p_{ace} = 193.19 Torr at 21 °C, for Q_{nit} = 100 sccm, a volumetric flow rate of Q_{ace} = 93.51 µl/min was expected. Experimentally, over two trials, 1760 ± 110 µl acetone was recovered at the solvent trap when nitrogen gas flowed at Q_{nit} = 100 sccm for 20 min and bubbled through acetone. This volume corresponds to Q_{ace} = 88 ± 5 µl/min. With a deviation of less than 10% between predicted and measured recovered solvent, it was assumed there were no significant leaks present in the system.

In a single channel configuration such as that described above, altering M_{nit} will alter the rate of swelling, but the equilibrium vapor pressure in the chamber will be the saturated vapor pressure of the solvent regardless of M_{nit}. The film is thus expected to swell to the same degree over a range of nitrogen mass flow rates. To lower the vapor pressure of the delivered solvent relative to the saturated vapor pressure and decrease degree of film swelling, mass flow of nitrogen through the solvent can be lowered while keeping the total nitrogen mass flow rate identical by using the second MFC to deliver additional nitrogen gas to the chamber (bypassing the second solvent container). The vapor pressure at the sample is then given by

$$p = p_{sol} \times M_{sol}/M_{nit,tot} \qquad \text{Eq 13}$$

where $M_{nit,tot}$ includes that delivered through the solvent as well as that delivered directly to the chamber.

A.3.2 Solvent Mixtures

Mixtures of solvents are appropriate for some experiments, including attaining order in diblock copolymer films and preparing aggregates of conjugated polymers.[76,89,152] Such solvent mixtures can be delivered to a sample using either a solvent mixture in a single reservoir or pure solvents in separate reservoirs. We demonstrated ability to control and monitor vapor pressure in each scenario for a mixture of acetone and chloroform.

To demonstrate the expected dependence of vapor volume ratio on liquid volume ratio, mixtures of acetone and chloroform were prepared in a single solvent reservoir and flow rate was set at Q_{nit} = 100 sccm. The generated vapors were condensed at the solvent trap and subsequently analyzed by gas chromatography. The resulting liquid–vapor equilibrium curve for acetone-chloroform liquid solvent mixtures is shown in Figure 31. The vapor volume ratio differs from the liquid volume ratio in accordance with the boiling points of each solvent and their interactions

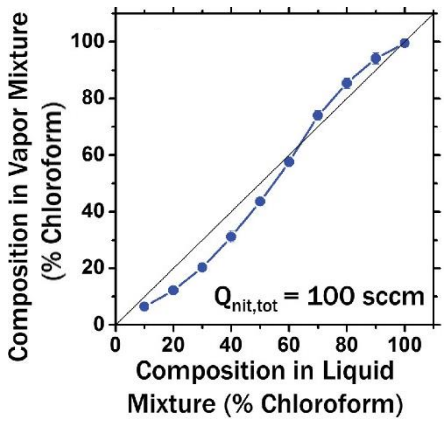

Figure 31. Liquid-vapor equilibrium curve for acetone-chloroform liquid solvent mixtures in a single reservoir. Error bars are standard deviations over 3 independent measurements, though most are smaller than the data points.

Appendix B. Simulation Method

This section provides details to the simulation method used in Chapter 2.

An *M* distribution similar to the experimental distribution (Figure 12b) was first generated: a Gaussian distribution of 1,000 random numbers centered at 0.52 with a standard deviation of 0.2 was generated. The lower and upper bounds of the distribution were set to 0 and 1, respectively. Then, 1,000 random numbers from a Gaussian distribution with mean value of 1 and standard deviation of 0.2 were generated, with these values representing the I_{max} values. Finally, I_{min} values were calculated using Eq 2 from the generated *M* and I_{max} values. These values were used for the simulation without noise. With no noise or quenching, the coefficients *a* and *b* in Eq 7 are simply equal to 4. Therefore, the *M* distribution at high excitation power is identical to that initially generated (Figure 15b).

Noise was introduced in the simulation by starting with a Gaussian distribution of 1000 random numbers with mean value of 0 and standard deviation of 0.04 and 0.08 for low and high excitation intensity, respectively. These random numbers were added to the original I_{max} and I_{min} values generated above and well-reproduced the signal:noise ratio seen experimentally. Using these new I_{max} and I_{min} values, the new *M* distributions were calculated using Eq 2 for both excitation intensities. The results are shown in Figure 15c and d.

To include quenching in the simulation, Eq 4 was used to calculate I_{max} and I_{min} values from the initial (noise-free) I_{max} and I_{min} values, i.e.,

$$I_{max}^{quenching} = I_{max} \times \frac{\alpha}{1 + \beta I_{max}} \qquad \text{Eq 14}$$

and

$$I_{min}^{quenching} = I_{min} \times \frac{\alpha}{1 + \beta I_{min}} \qquad \text{Eq 15}$$

α and β values of 1 and 0.2 were used, respectively, as these values well-reproduced the experimental data. New *M* and *M'* values were then calculated following Eq 2 at both low and high excitation powers. These results are shown in Figure 15e and f. Finally, Figure 16 in Chapter 2 was produced by adding both quenching and noise into the simulation in that order. New *M* and *M'* values were then calculated following Eq 2 at both low and high excitation powers using the newly calculated I_{min} and I_{max} values after applying quenching and noise.

Appendix C. Calculation of Single Molecules per Aggregate

This section provides details to the calculation method used in Chapter 3.

The number of single molecules per aggregate, $N_{\text{SM-AGG}}$ was calculated via

$$N_{SM-AGG} = \frac{\frac{1}{I_{SM,B}}\left\{I_{film,B} - \frac{1}{C}\left(I_{film,A} - \sum_1^{N_{AGG}} I_{AGG}\right)\right\}}{N_{AGG}} \qquad \text{Eq 16}$$

Here, N_{AGG} is the number of aggregates within the imaging area, $I_{\text{SM,B}}$ is the median fluorescence intensity of a single chain before SVA, $I_{\text{film,B}}$ is the total intensity of the fluorescence image before SVA, $I_{\text{film,A}}$ is the total intensity of the fluorescence image after SVA, ΣI_{AGG} is the sum of fluorescence intensities from aggregates within an imaging area. *C* is a correction factor that was used previously to account for decreased fluorescence intensity from the background of films after solvent vapor annealing.[79] In our previous publication on aggregates formed from MEH-PPV initially dissolved in toluene, the decrease was attributed to enhanced compaction of single molecules remaining in the background and contributing to total film intensity after SVA. Here, given the set of findings described in Chapter 3, this correction factor is obtained from concentration A and accounts for the presence of small aggregates in the background of films C and D following SVA. *C* is set to 1 for aggregate B and is set to 0.82 for aggregates C and D, with this obtained from the median intensity of features in films of concentration A before and after SVA, assuming two molecules per aggregate. We note that 0.82 may be an overestimate of the correction factor if there is more aggregation and quenching in the background of films C and D than that which occurs in films of concentration A, which in turn would lead to an overestimate of the number of chains per aggregate in concentrations C and D. We thus consider the numbers presented in Chapter 3 to be upper bounds on the number of chains per aggregate.